Comparative Structure Based Virtual Screening Utilizing Optimized AlphaFold Model Identifies Selective HDAC11 Inhibitor

Fady Baselious [1], Sebastian Hilscher [1], Dina Robaa [1], Cyril Barinka [2], Mike Schutkowski [3] and Wolfgang Sippl [1,*]

[1] Department of Medicinal Chemistry, Institute of Pharmacy, Martin-Luther-University of Halle-Wittenberg, 06120 Halle (Saale), Germany.
[2] Institute of Biotechnology of the Czech Academy of Sciences, BIOCEV, 252 50 Vestec, Czech Republic.
[3] Charles Tanford Protein Center, Department of Enzymology, Institute of Biochemistry and Biotechnology, Martin-Luther-University of Halle-Wittenberg, 06120 Halle (Saale), Germany.
* Correspondence: E-mail: wolfgang.sippl@pharmazie.uni-halle.de

Abstract: HDAC11 is a class IV histone deacylase with no crystal structure reported so far. The catalytic domain of HDAC11 shares low sequence identity with other HDAC isoforms which makes the conventional homology modeling less reliable. AlphaFold is a neural network machine learning approach that can predict the 3D structure of proteins with high accuracy even in absence of similar structures. However the fact that AlphaFold models are predicted in absence of small molecules and ions/cofactors complicate their utilization for drug design. Previously we optimized an HDAC11 AlphaFold model by adding the catalytic zinc ion and minimization in the presence of reported HDAC11 inhibitors. In the current study we implement a comparative structure-based virtual screening approach utilizing the previously optimized HDAC11 AlphaFold model to identify novel and selective HDAC11 inhibitors. The stepwise virtual screening approach was successful in identifying a hit that was subsequently tested using an in vitro enzymatic assay. The hit compound showed an IC_{50} value of 3.5 μM for HDAC11 and could selectively inhibit HDAC11 over other HDAC subtypes at 10 μM concentration. In addition we carried out molecular dynamics simulations to further confirm the binding hypothesis obtained by the docking study. These results reinforce the previously presented AlphaFold optimization approach and confirm the applicability of AlphaFold models in the search for novel inhibitors for drug discovery.

Keywords: AlphaFold; HDAC11; virtual screening; modelling; in vitro assay; pharmacophore; docking; molecular dynamics simulation

1. Introduction

Histone deacetylases (HDACs) form a protein family responsible for catalyzing the elimination of acetyl groups from lysine residue of histone proteins as well as other substrates [1]. Histone deacetylase family is classified into four main classes, three of which are constituted by eleven zinc dependent HDACs, namely class I (HDAC1, 2, 3 and 8), class IIa (HDAC4, 5, 7 and 9), class IIb (HDAC6 and 10) and class IV (HDAC11) [2].

HDAC11, the sole member of class IV of HDACs family, is the smallest member of the family and one of the least studied HDAC subtypes [3,4]. It is expressed in multiple organs including heart, kidney, brain tissues, skeletal muscles and gall bladder [4,5]. Evidence demonstrated that HDAC11 is involved in various physiological processes such as modulation of immune system [6,7] and maintaining genomic integrity [8]. It was also evident that HDAC11 is connected to some pathological processes and represents a potential target for the treatment of several diseases including multiple sclerosis, viral infections and obesity-related diseases [9-11]. HDAC11 was also found to be involved in the modulation of cancer growth and is overexpressed in different cancer forms [12-19]. For example, inhibition of HDAC11 showed beneficial effects in neuroblastoma cells [20] suggesting that HDAC11 represents a promising target for the treatment of some cancer forms.

A robust deacetylase activity was found for HDAC11. It is more than 10,000-fold more efficient than the deacetylase activity, suggesting that this activity may be the major activity of the enzyme in vivo [21-23].

To date, only a few selective HDAC11 inhibitors have been reported. Hydroxamic acid based inhibitors include FT895 [24], the only weakly active MIR002 [25] and the recently developed inhibitor BP94 [26]. FT895

showed beneficial effects in reducing non-small cell lung cancer cells viability [27], while BP94 could ameliorate neuropathic pain in mouse model [26]. Due to its preference to remove long-chain fatty acyl groups, it has been postulated that HDAC11 contains a hydrophobic pocket near its catalytic Zn2+ center. Therefore, inhibitors containing long alkyl chains have been described. For example, SIS17 [28] which contains an alkyl hydrazide moiety and inhibits HDAC11 in vitro in the submicromolar range. Alkyl hydrazides have also recently been described for other HDACs, such as HDAC3 and HDAC8, as novel zinc binding groups. [29,30]. Similarly, the trapoxin A analog TD034 [31] possesses a long alkyl chain that might be the reason for the observed HDAC11 selectivity [31].

No crystal structure of HDAC11 has been reported and its catalytic domain shows low sequence identity (<30%) when compared to the primary sequences of the catalytic domains available in the PDB databank for other human HDAC isoforms. This fact complicates the conventional template-based homology modeling [32].

AlphaFold is a neural network machine learning approach for predicting the 3D structures of proteins with atomic accuracy even in absence of known similar structures [33]. A database containing the 3D structures of the whole human proteome was built by AlphaFold [34]. The models from AlphaFold should be carefully considered when used for structure-based drug design studies because the folding is predicted in absence of small molecules like water molecules, ligands and cofactors.

In a recent study by Ren et al. [35] AI driven molecular generation was combined with utilization of AlphaFold model for the aim of drug discovery for cyclin dependent kinase 20 (CDK20). In this study, modification of the AlphaFold model by removing the C-terminus which was blocking the solvent exposed region of the protein and occupying the ATP binding pocket through Arg305 was performed in order to make the model usable. In another study, Zhu et al. [36] utilized a similar approach to successfully design new inhibitors for salt inducible kinase 2 (SIK2).

The two studies discussed above used AlphaFold models for protein targets sharing reliable sequence identity with other proteins within the same family for which crystal structures are available and utilized AI driven molecular generation techniques rather than docking. Several other studies addressed the usability of AlphaFold models for docking [37-41] and real world virtual screening scenarios [39,42,43]. One of these studies assessed the usability of AlphaFold structures predicted while excluding structural templates with more than 30% identity thus imitating virtual screening process with a model based on low prior structural information. Results from these studies demonstrated a worse performance of the AlphaFold models compared to crystal structures suggesting that using unmodified AlphaFold models is not an ideal scenario. This worse performance could be due to the collapse or distortion of the binding site resulting from minor variation at the side chain level or larger variation of the backbone, suggesting post-modeling or optimization is required to obtain more realistic holo models [38-43].

In agreement with these results, it was demonstrated that optimization of the binding site by inducing flexibility or manual modification of the low confidence regions could enhance the docking results [37,39,40,44]. In our recent work, we showed that binding site optimization of HDAC11 AlphaFold model by adding the catalytic zinc ion and performing minimization in the presence of transplanted ligands resulted in a model that could be used for docking of the known selective HDAC11 inhibitors FT895, MIR002 and SIS17 [32].

In the current study, we present an application for using optimized AlphaFold models for virtual screening while addressing HDAC subtype selectivity [45]. We demonstrate herein, that our previously optimized HDAC11 AlphaFold model was successfully utilized for picking a selective hit through comparative virtual screening approach. In the developed multistep screening, various approaches including structure based pharmacophore screening as pre-filtering of large databases, ligand docking, pose filtering and prioritization were applied as described in the Methods section. To experimentally confirm the virtual screening results the most promising hit was synthesized and tested in vitro using different HDAC subtypes. In addition, we analyzed the predicted binding mode from docking by means of molecular dynamics (MD) and MetaDynamics simulations.

2. Results and Discussion

2.1. Dataset selection and curation:

Hydroxamates comprise well defined and characterized pharmacophore for HDAC inhibitors and considered the most commonly used zinc binding group in HDAC inhibitors [46,47]. Some of the inhibitors bearing the hydroxamate scaffold as vorinostat (SAHA), belinostat (PXD-101) and panobinostat (LBH589) have been

approved by the FDA in the past for the treatment of hematological malignancies [48]. Benzohydroxamates constitute an important class of HDAC inhibitors and their development entail an active field within inhibitors design for several HDAC subtypes [47]. ZINC20 is a publicly available database that includes nearly two billion compounds in 2D and 3D downloadable formats through a website that allows for rapid analogue search [49]. Initially, a focused database of 407834 benzohydroxamates was acquired from the ZINC20 database. The library was further prepared with generating possible ionization states at physiological pH 7.0 ± 2.0. The preparation step resulted in library that contained 510529 ligands with various ionization states which was then subjected to filtration to select the ligands with hydroxamate state only. The Lipinski rule of five is an important early measure for identifying bioavailable drug like candidates. According to this rule the compound must possess the following properties: molecular weight <500 Da, logP <5, H-bond donors <5, and H-bond acceptors <10. To further select drug like molecules the prepared library was filtered to remove any molecule that violate Lipinski's rule of five [50,51]. The initial curation resulted in a library of 18,113 ligands. The multistep virtual screening process was then performed as presented in the workflow (**Figure 1)**.

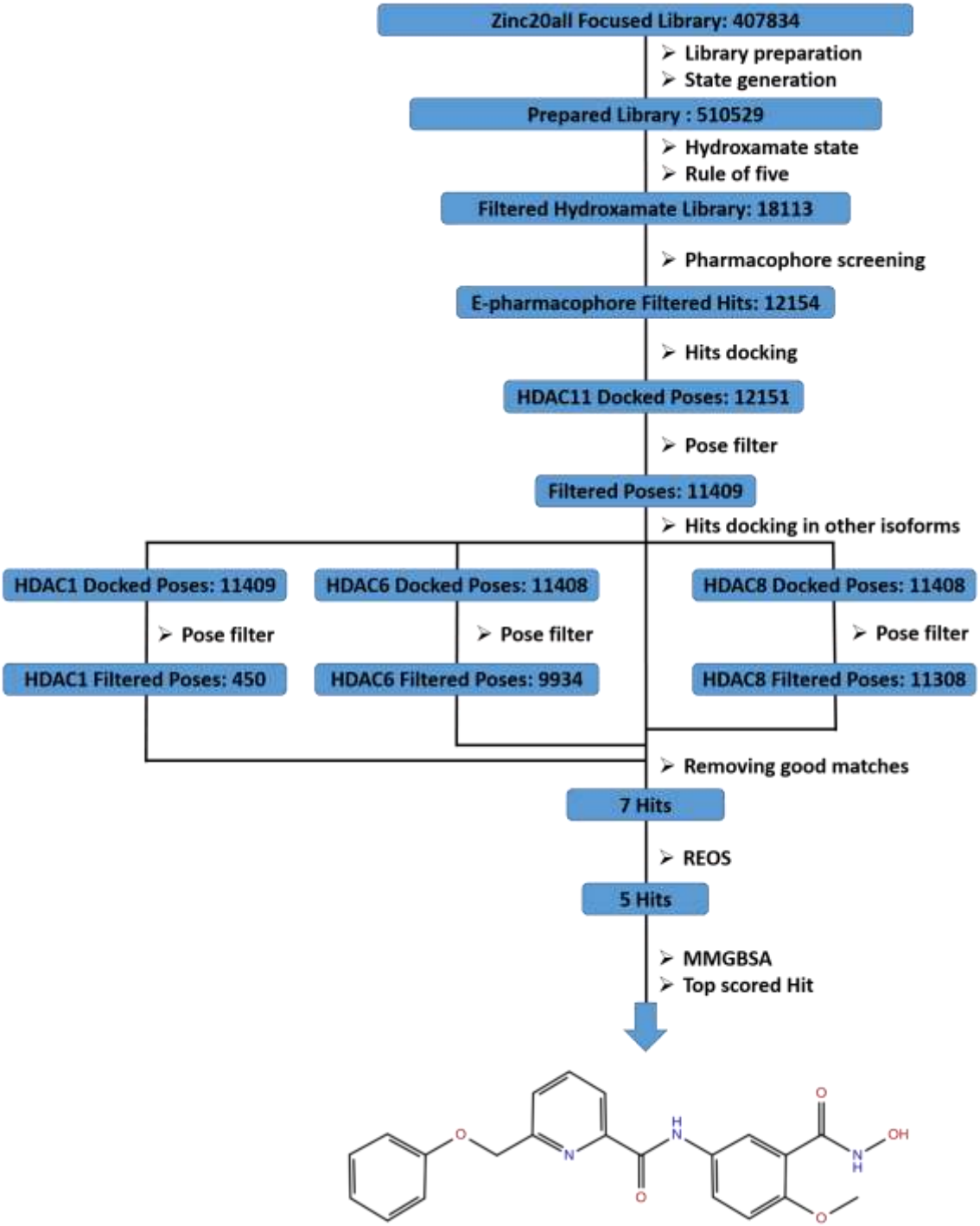

Figure 1. Workflow of the stepwise virtual screening.

2.2. Virtual screening:

The E-pharmacophore module implemented in Phase automatically generates a pharmacophore hypothesis that is based on the complementarity of the protein and ligand features from a protein-ligand complex. This involves using Glide XP scoring terms to determine which features contribute the most to the binding. The hypothesis obtained from using the previously optimized complex of TSA and HDAC11 AlphaFold model exhibited four features (**Figure 2**), namely a hydrogen bond acceptor feature assigned for the carbonyl-O, a hydrogen bond donor assigned to the NH and negative feature for the deprotonated hydroxyl group of the hydroxamate zinc binding group as well as an aromatic feature for the phenyl capping group. Excluded volumes that are based on the occupation of space by protein atoms were also added. Pharmacophore screening was performed to select the ligands that matched the four features, with the aim of filtering out very small ligands/fragments as

well as compounds larger than they could be accommodated in the HDAC11 pocket. Thus, the pharmacophore formed by the excluded volumes was primarily used to reduce the very large number of compounds for the subsequent, more computationally demanding docking method.

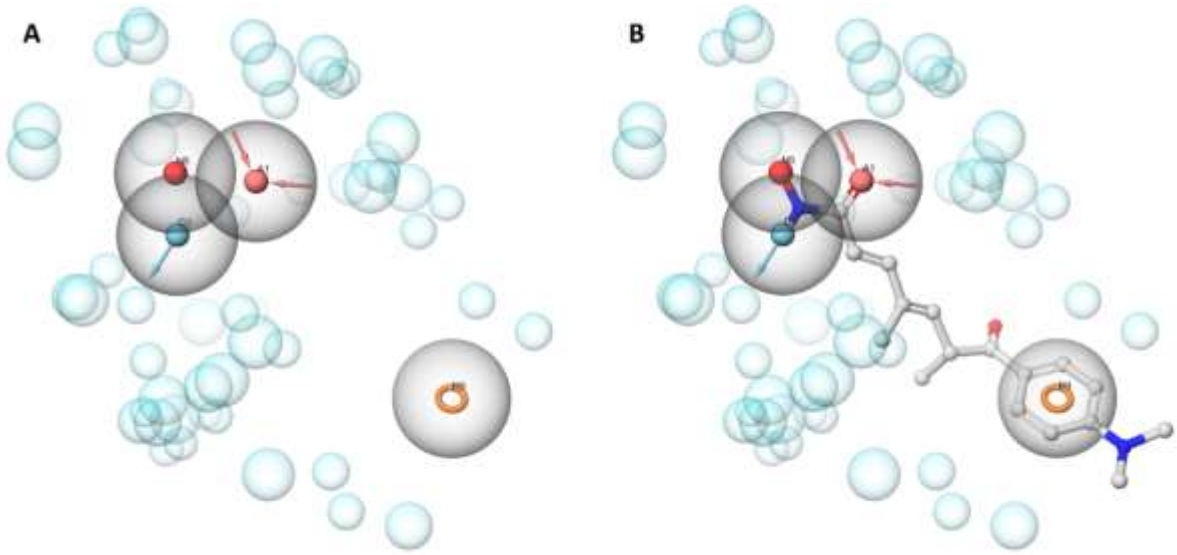

Figure 2. E-pharmacophore model. (**A**) Pharmacophore features: HB donor represented as cyan sphere, HB acceptor as pink sphere, negative as red sphere and aromatic as orange ring. Excluded volumes are represented as cyan transparent spheres and feature matching tolerance as grey transparent spheres. (**B**) Superposition of the inhibitor TSA on the features of the generated hypothesis. Ligand is represented as grey sticks.

The pharmacophore screening step was effective and could filter out 5959 compounds. Docking-based virtual screening of the remaining 12154 structures was then performed using the grid generated from the HDAC11-TSA optimized AlphaFold model. In our previous study, we were successful to obtain four optimized complexes by minimization of the HDAC11 AlphaFold model with previously reported active ligands of HDAC11 for which X-ray crystal structures with HDAC8 are available in the protein data bank (PDB). The selection of the TSA-HDAC11 complex for the virtual screening was based on the results obtained from the previous study since it showed the best performance regarding the docking of the selective inhibitor FT895 (**Figure 3**) and was further utilized in docking of other selective inhibitors as MIR002 and SIS17. Almost all of the hits from the pharmacophore screening step could pass the docking based screening. Furthermore, filtration of the obtained docking poses was performed to select the ligands that can show a bidentate chelation mode to the catalytic zinc ion. Pose filtration was performed utilizing the distances between the chelator carbonyl and hydroxyl oxygen atoms of the hydroxamate moiety to the zinc ion. Compounds showing distances more than a cut off of 2.6 Å between any of the chelator atoms and the zinc ion were removed.

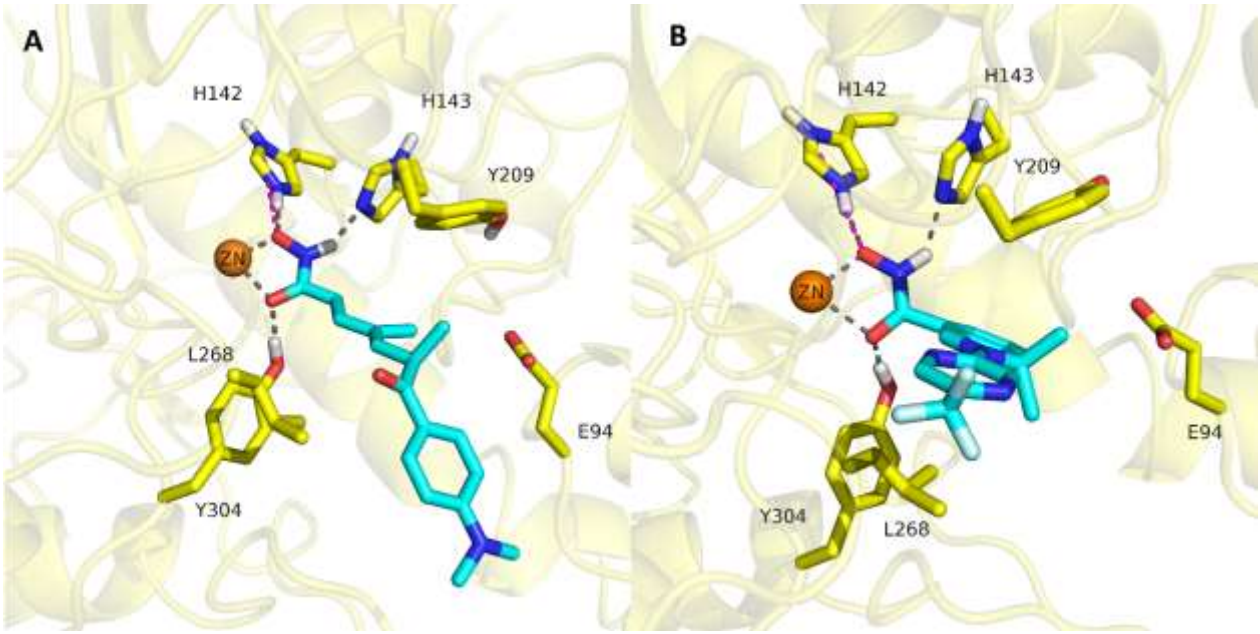

Figure 3. (**A**) Minimized pose of TSA in HDAC11 optimized AlphaFold model. (**B**) Docked pose of FT895 in the optimized HDAC11 AlphaFold model. The protein backbone is represented as yellow cartoon, the interacting binding site residues as yellow sticks, zinc ion as orange sphere and the ligands as cyan sticks. Hydrogen bonds and coordination bonds are represented as grey dashed lines and ionic interactions as magenta dashed lines.

For the aim of searching for selective HDAC11 ligands, a comparative docking-based virtual screening approach was then applied. The hits obtained from the docking in HDAC11 which could pass the pose filtration step were then screened by docking into HDAC1, HDAC6 and HDAC8 crystal structures. The obtained hits from every screening were further subjected to pose filter screening. Ligands which could show correct docking pose with bidentate chelation of the catalytic zinc ion in any of HDAC1, HDAC6 and HDAC8 were removed from the HDAC11 hit list. For HDAC6, ligands which could chelate the zinc ion in a monodentate fashion were also removed. This step was very effective and could filter out most of the compounds leaving only 7 compounds (**Table S1, Supplement)** that could show a correct chelation mode in HDAC11 but not in any of the other isoforms.

Rapid elimination of swill (REOS) [52,53] filter was then applied to remove compounds containing reactive or toxic moieties which might also interfere with biological assays. Two compounds containing nitro groups were removed by using this filter. Interestingly, the final five hits (**Table 1**) are all bearing a methoxy, ethoxy or chloro substituent on the ortho position of the hydroxamate moiety which indicates that substitution at this position might represent a selectivity determinant for HDAC11 inhibition.

Table 1. Final hits and MM-GBSA dG binding values.

Title	Structure	MM-GBSA dG bind
ZINC000028464438 (**9**)	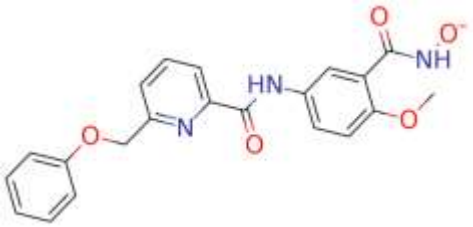	-49.76
ZINC000671998736	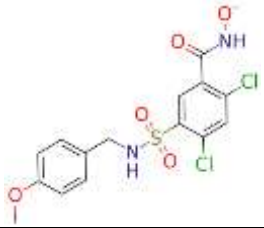	-39.75

ZINC000742823399	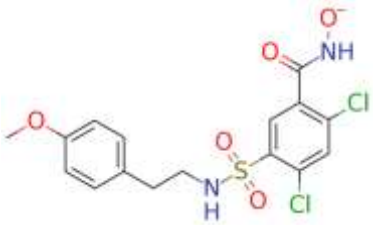	-48.68
ZINC000916666211	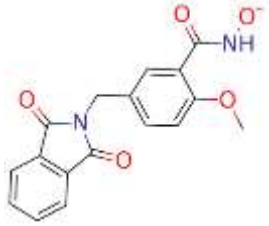	-48.21
ZINC000916666264	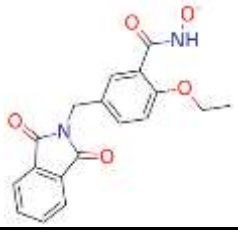	-41.45

In the last step of the virtual screening workflow the five final hits were prioritized through MM-GBSA calculations. MM-GBSA calculations showed that the top ranked molecule is ZINC000028464438 (**9**) which is bearing a methoxy group as ortho substitution to the hydroxamate moiety and an amide linker in the meta-position. It is worth noting that a selective HDAC11 inhibitor (PB94) was recently presented by Bai et al. [26]. Based on the structure activity relationship, the authors reported that a methoxy group in the ortho position of their developed benzohydroxamate inhibitors is a key factor for HDAC11 selectivity which is in agreement with our results from the virtual screening.

2.3. In vitro enzymatic evaluation:

Due to the unavailability of the top-ranked hit ZINC000028464438 we decided to resynthesize the compound (**9**) as reported [54], purified it, confirmed the structure by NMR and MS and tested it at a concentration of 10 μM against HDAC11 as well as all other HDAC subtypes (HDAC1-10) to determine the selectivity. The synthesis and analytical characterization described in detail in Methods section. Compound **9** showed inhibition of the enzymatic activity of around 85 % for HDAC11 while it showed almost no inhibition for nearly all HDAC subtypes and only around 20 % inhibition of HDAC6 (**Figure 4A**). Interestingly, the findings from the in vitro screening confirms the results obtained from the theoretical study as the hit compound was not able to adopt reasonable poses in any of HDAC1, HDAC6 and HDAC8. On the other hand, a perfect pose with bidentate chelation mode that was also showing the expected interactions of a benzohydroxamate based HDACs inhibitor was observed in HDAC11 and proved to be stable during MD simulations. These results further confirm that HDAC11 can accommodate such bulkier substitutions in the ortho position of the benzohydroxamate moiety of the inhibitor providing a unique feature that can be used to target isoform selectivity when designing new inhibitors.

Furthermore, the IC_{50} for HDAC11 was determined to be about 3.5 μM **(Figure 4B**). While this virtual screening hit showed only moderate HDAC11 inhibitory activity, it still can be considered a promising hit compound due to the good selectivity. Further chemical optimization is required that might include manipulation of the size and structure of the ortho substituent at the benzohydroxamate moiety, changing the position and structure of the amide linker or changing the structure and decorations of the capping group. The obtained results can be assessed in the light of capabilities of virtual screening and the role it plays for hit identification and finding new scaffold leads by screening of large compound libraries, a process that is commonly followed by lead optimization. We included the well characterized HDAC11 inhibitor SIS17 as a reference compound in our enzyme inhibition assay and it showed IC_{50} of 0.17 μM which is in line with reported data [28] (**Figure 4A and Supplement S6**).

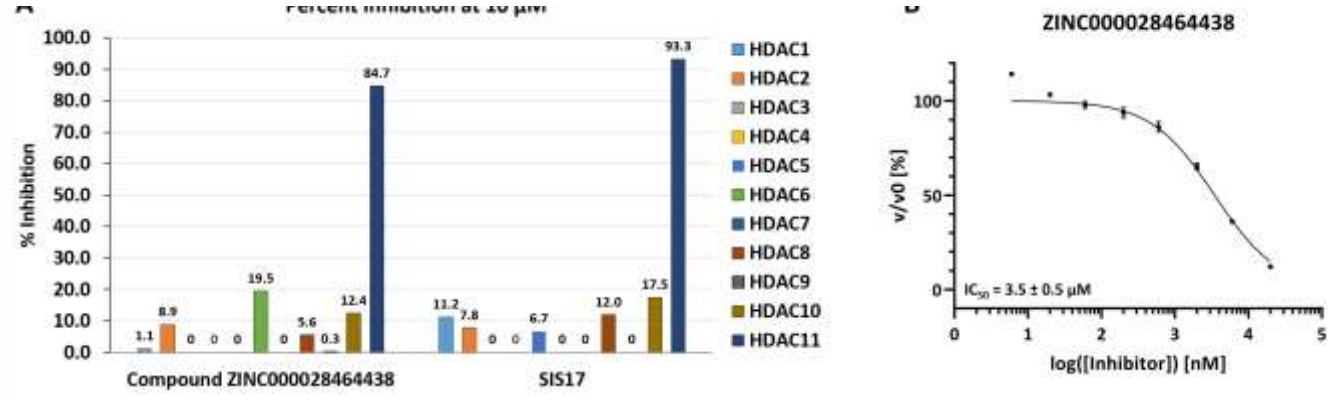

Figure 4. (**A**) Relative inhibition of enzymatic activity for all HDAC subtypes at 10 µM of **9** (ZINC000028464438) and SIS17. (**B**) Determination of IC_{50} value of **9** (ZINC000028464438) for HDAC11.

2.4. Analysis of the docked poses:

Analyzing the docked poses of the confirmed hit revealed that the obtained pose of the hit compound in the optimized HDAC11 AlphaFold model **(Figure 5**) showed bidentate chelation with distances of 2.41 Å and 2.17 Å between the zinc ion and the carbonyl and hydroxyl oxygen atoms of the hydroxamate moiety, respectively. A salt bridge to His142 as well as hydrogen bond interactions with His143 and Tyr304 were observed. The ligand also demonstrated $\pi-\pi$ interactions between the phenyl ring of the benzohydroxamate and His183. The phenoxymethyl capping group adopts a bent conformation and is directed towards loop1. For HDAC1 the hit ligand showed a pose in which no metal chelation was observed as the hydroxamate moiety could not reach the zinc ion in the depth of the binding pocket but barely reaching to His178 with which the ligand forms hydrogen bond through the hydroxyl oxygen of the hydroxamate moiety. Another hydrogen bond was observed between the NH of the amide linker and Asp99 side chain. In HDAC6, the docking resulted in a flipped orientation with the hydroxamate moiety facing the solvent which indicates that the ligand could not fit into the binding site. No interactions could be observed for the obtained pose in HDAC6. The hit ligand could not show the bidentate zinc chelation commonly observed for cocrystallized HDAC8 inhibitors.

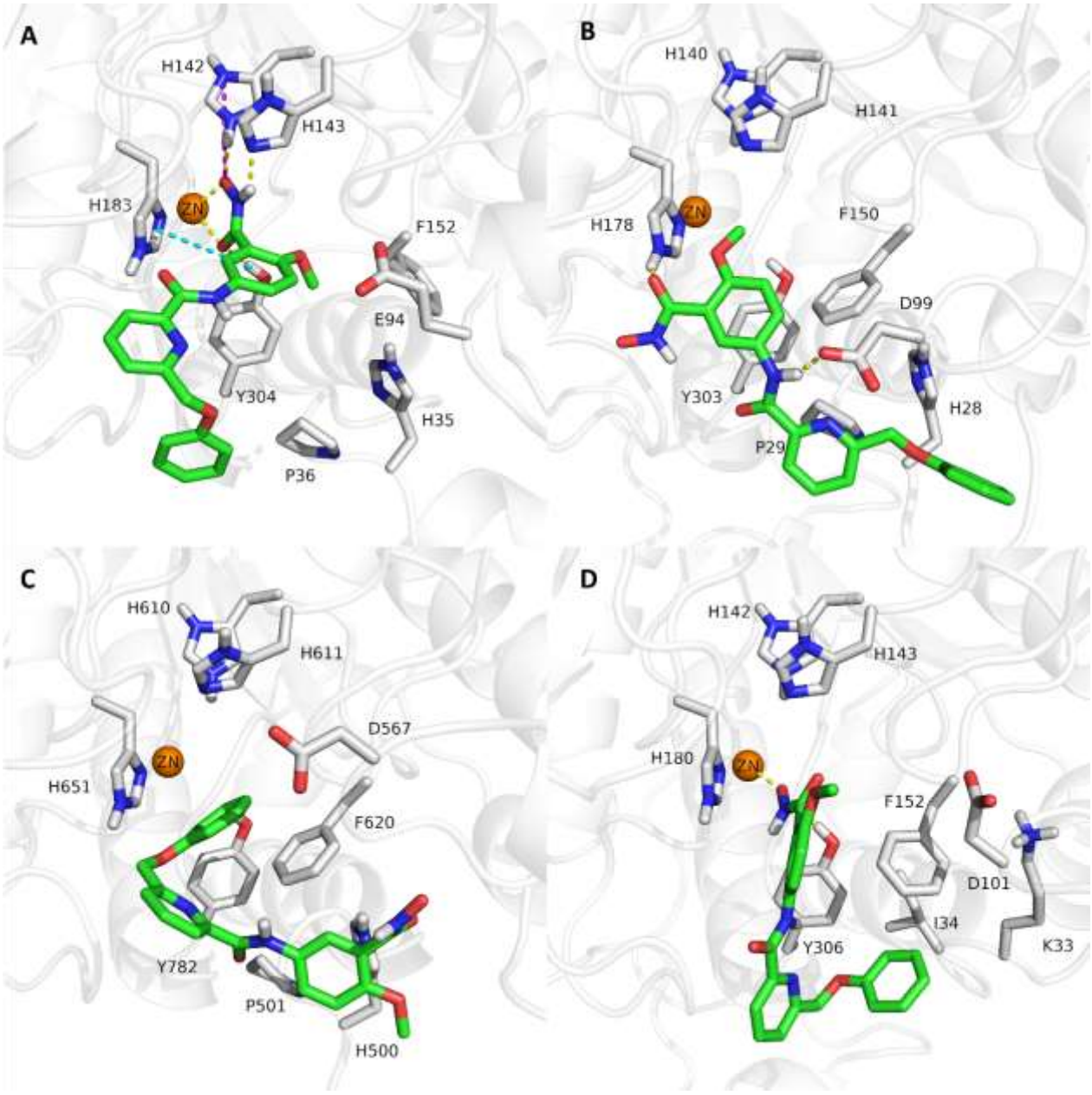

Figure 5. Docked poses of ZINC000028464438 (**9**). (**A**) HDAC11. (**B**) HDAC1. (**C**) HDAC6. (**D**) HDAC8. The protein backbone is shown as white cartoon, zinc ion as orange sphere, the binding site residues as grey sticks and the ligands as green sticks. Coordination and hydrogen bonds are shown as yellow dashed lines, π –π interactions as cyan dashed lines and the ionic interactions as magenta dashed lines.

In previous studies, we performed a structural comparison of the optimized HDAC11 AlphaFold model with HDAC6 and HDAC8 as candidates of class I and class II HDACs [32]. The comparison showed that the folding of loop three of HDAC11 is more similar to HDAC8 suggesting the formation of the so called foot pocket in HDAC11 similarly to HDAC8. Thus the HDAC11 model shows a large foot pocket that justifies the binding of ligands with long alkyl chains such as the alkyl hydrazide derivative SIS17. The entrance of the foot pocket in HDAC11 is formed by the residues Gly139, Gly140 and Phe141, whereas in HDAC8 the Phe141 is replaced by the bulkier residue Trp141. In HDAC6, loop 3 residues are replaced by the bulkier Pro607 and Pro608 as well as the larger residue Arg606. In addition the Arg606 side chain is directed towards loop 1 forming polar interactions with Glu50 thus causing loop 3 to fold into the opposite direction and blocking the formation of the foot pocket in HDAC6.

Since we found that the optimized HDAC11-AlphaFold model in complex with TSA and the lowest energy rotamer of Phe152 (flipped out conformation) showed the best results in docking of selective ligands such

as FT895 and SIS17, we used this model for virtual screening in the current study. To better understand the structural basis of the HDAC11 inhibition, we analyzed the shape of the binding pockets of the crystal structures and the HDAC11 AlphaFold model. The analysis revealed that the flipping of Phe152 in HDAC11 together with the less bulky residue Phe141 as foot pocket gatekeeper allows for a wider binding pocket that can accommodate the bulky methoxy substituent in the ortho position of the benzohydroxamate moiety of the hit **9**. Analysis of the crystal structures of HDAC1 (5ICN) and HDAC6 (5EDU) (**Figures 6A and 6B**) shows that here the different conformation of this conserved phenyl alanine brings it closer to the residues from loop 1 and loop 2 (such as Tyr24 and Lys31 in HDAC1 and Glu502 in HDAC6) and narrowing the pocket in HDAC1 as well as HDAC6. As a result this pocket cannot accommodate ortho-substituted benzohydroxamates (no zinc chelation possible) like the hit compound **9.**

The HDAC8 crystal structure 5FCW was used as an "anti-target" for virtual screening in this study, as to our knowledge it has the best resolution for a wild-type human HDAC8 crystal structure co-crystallized with a hydroxamic acid. A closer look and comparison of the docked poses of the hit compound in HDAC11 and HDAC8 show that the ligand in the HDAC11 pocket is oriented slightly differently (**Figure 6C and 6D**), allowing for a better fit to the ortho substitution. Another observation is that in the docking poses in HDAC8, a considerable portion of the ligand is exposed to the solvent due to the shorter loop 1 of HDAC8, whereas the ligand in HDAC11 is stabilized by the longer loop 1, as shown in the MD studies. In case of HDAC8 selective inhibitors a more L-shaped conformation was observed in docking studies and X-ray structures [45,55,56]. Consideration of these observations may explain the preferential binding of the hit compound in HDAC11.

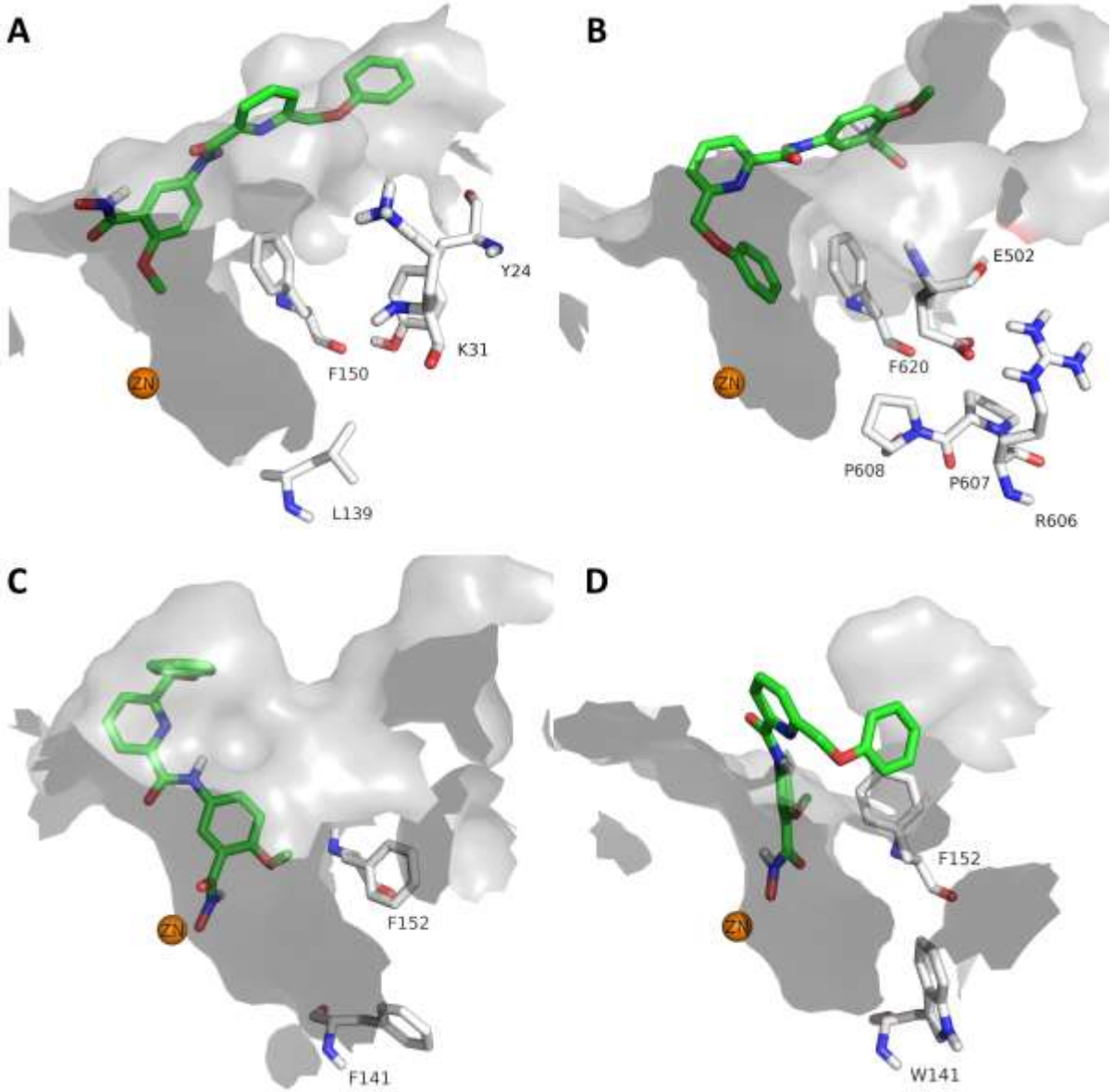

Figure 6: Docking poses of the hit compound **9** and demonstration of the binding site shape and size. (**A**) HDAC1 (PDB ID 5ICN), (**B**) HDAC6 (PDB ID 5EDU), (**C**) HDAC11 (AlphaFold model), (**D**) HDAC8 (PDB ID 5FCW).

2.5. Molecular dynamics simulations:

Docking methods are limited by not considering the flexibility of the protein but treating the receptor as rigid body. On the other hand, MD simulation technique takes into account the flexibility of the complex thus giving a deeper insight regarding the binding mode of the ligand and its behavior in dynamic environment. Therefore we decided to study the binding mode of the confirmed hit extensively using short and long MD simulations. The docking pose of the hit compound in the optimized HDAC11 AlphaFold model was subjected to three short (50 ns) molecular dynamics simulations using different random seeds. Furthermore, a longer MD simulation (500 ns) was performed to assess the stability of the obtained pose over a longer time scale.

In all MD simulations the protein and the zinc ion demonstrated high stability that could be observed through the calculated RMSD plots. The protein backbone is stabilizing between 1 Å and 2 Å while the zinc ion is stabilizing almost at 1 Å (**Figures 7A and 7B**).

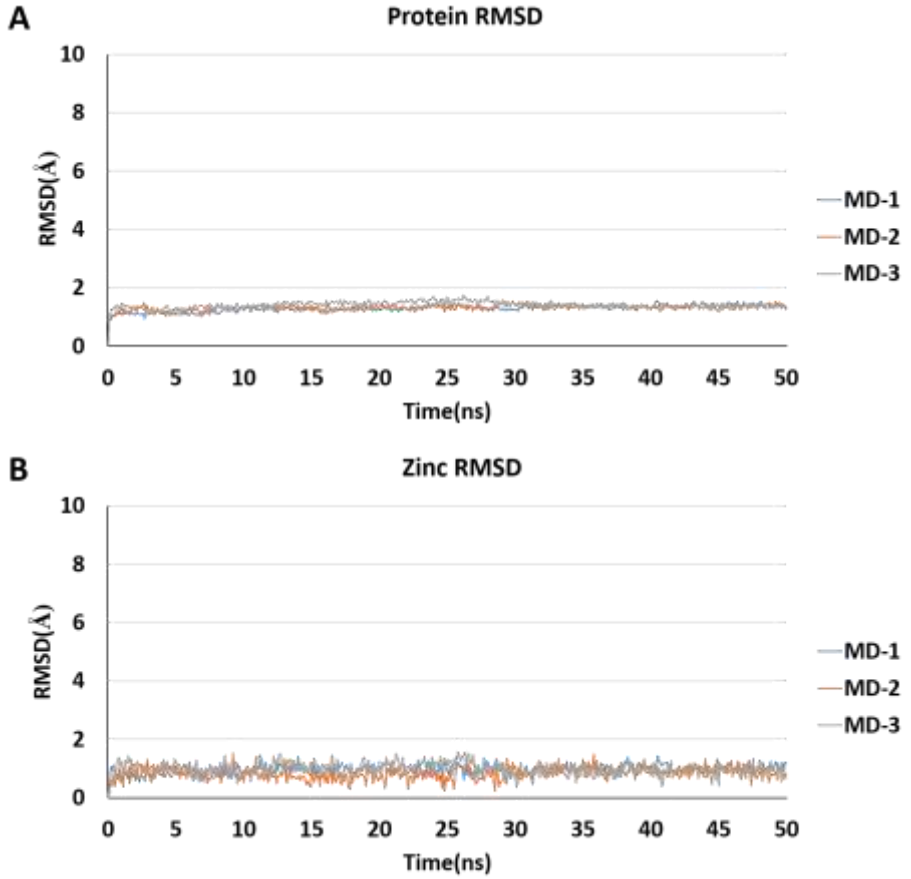

Figure 7. RMSD plots of ZINC000028464438 (**9**) for 3 repeated MD runs each for 50 ns. (**A**) RMSD plots of protein backbone heavy atoms. (**B**) RMSD plots of zinc ion.

The results of the three independent short MD simulations were comparable. The RMSD plot of the ligand demonstrated that there is a shift in the pose directly after the simulation started and that the ligand is stabilizing between 3 Å and 4 Å till the end of the simulation (**Figure 8A**). Analyzing the RMSF of the ligand heavy atoms showed that the phenoxymethyl capping group is the most fluctuating substructure of the ligand and with an RMSF reaching 2 Å (**Figure 8B**).

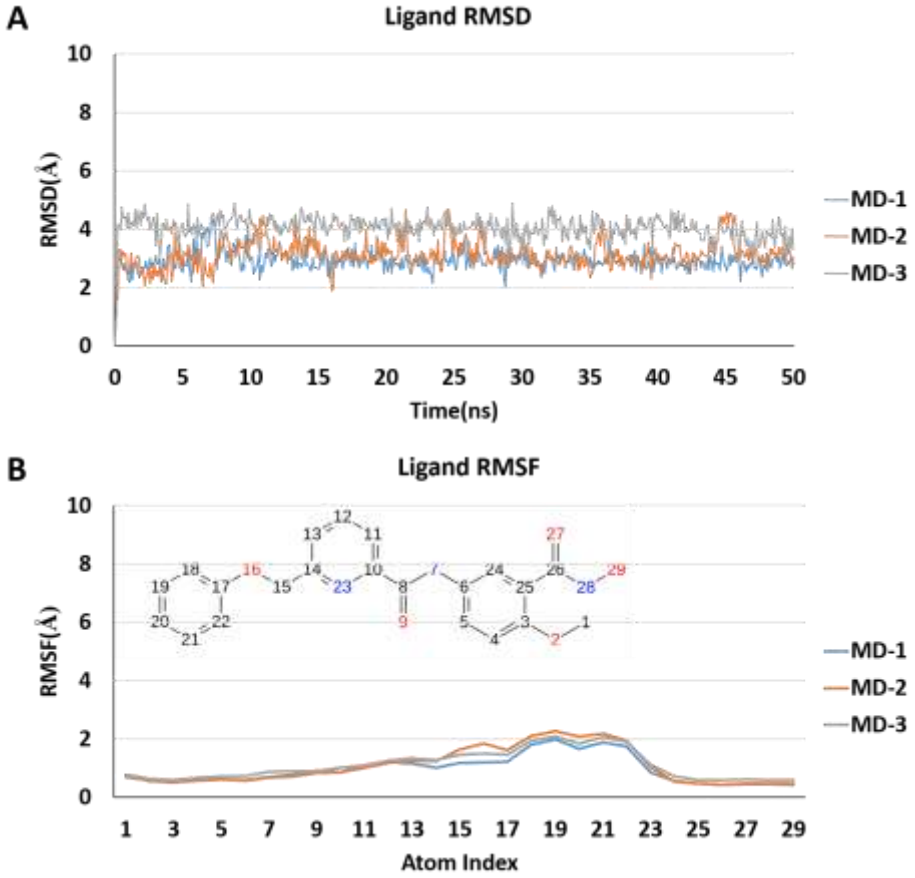

Figure 8. RMSD and RMSF plots of ZINC000028464438 (**9**) for 3 repeated MD runs each for 50 ns. (**A)** RMSD plots of ligand heavy atoms. (**B)** RMSF plots of ligand heavy atoms.

Inspecting the MD trajectories showed that there is a slight shift of the initial docking pose allowing for the benzohydroxamate moiety to be accommodated deeper into the binding pocket which leads also to a better accommodation of the capping group through the relaxation of the conformation (**Figure 9**).

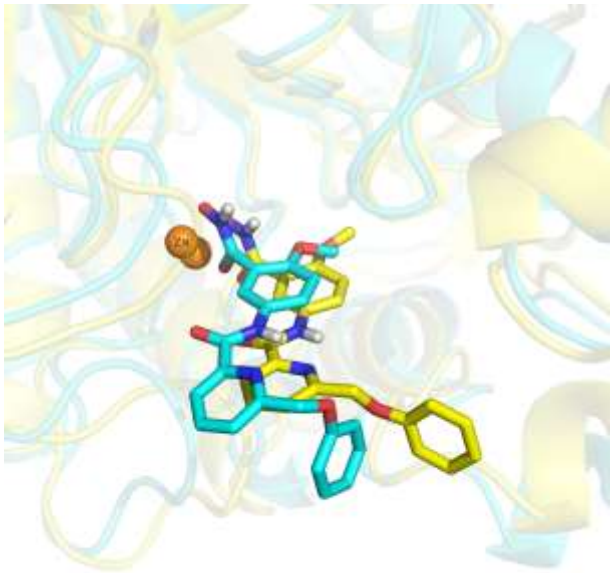

Figure 9. Superposition of the first and last frames of ZINC000028464438 (**9**) showing the shift in the pose during the simulation from the first MD run of 50 ns. The zinc ion is represented as orange sphere, the protein backbone as cartoon and ligand as sticks. The protein backbone and the ligand are colored in cyan and yellow for the first and last frames, respectively.

The stability of the bidentate chelation mode was confirmed for the three runs by monitoring the distances between the chelator atoms of the hydroxamate zinc binding group and the zinc ion (**Figures 10A and 10B**). The salt bridge to His142 showed very high stability with persistence of almost 100% for the three runs. The hydrogen bond interaction to His143 showed moderate stability with persistence ranging between 54% and 72%. It is worth noting that we observed such week to moderate stability of the hydrogen bond interaction to His143 during MD simulation with some of the ligands we utilized for the model optimization in our previous study as TSA and also with some of the selective docked ligands as FT895 and MIR002 [32].

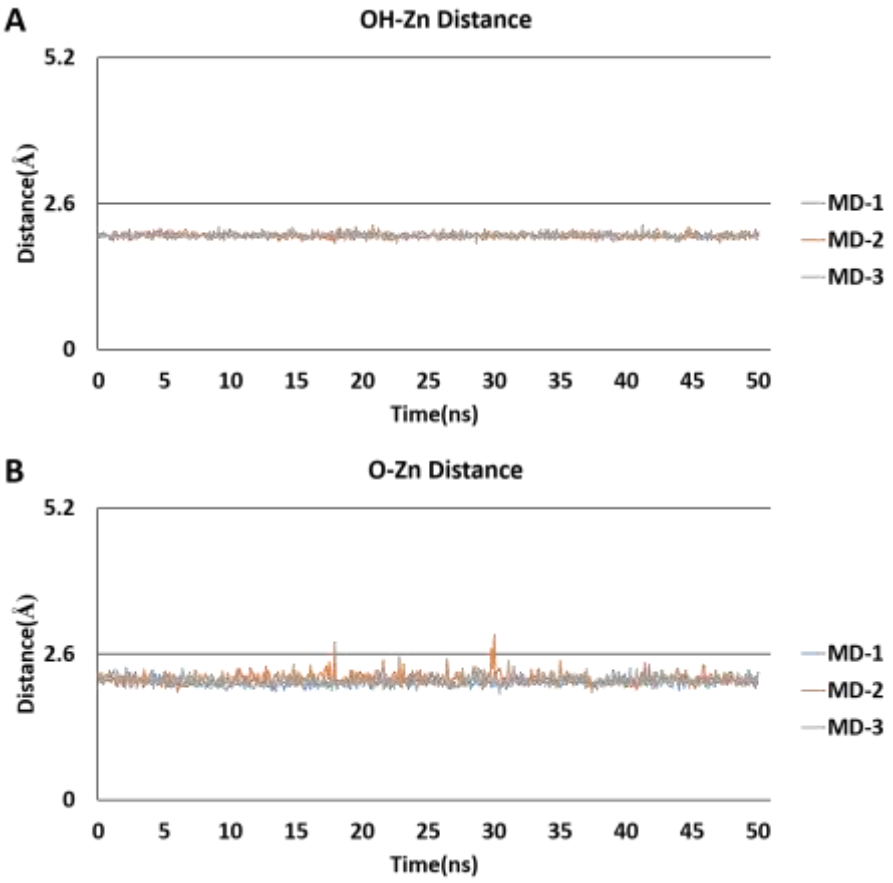

Figure 10. (**A**) and (**B**) Distances to the zinc ion for three repeated MD runs each for 50 ns for the hydroxyl and the carbonyl oxygen atoms of the hydroxamate zinc binding group, respectively.

The slight shift in the pose discussed above leads to almost complete loss of the hydrogen bond between Tyr304 and the carbonyl oxygen of the hydroxamate moiety but allowed for the formation of another hydrogen bond between the same residue and the oxygen of the methoxy substituent in the ortho position of the benzohydroxamate substructure that showed high stability with persistence ranging between 72% and 87%. This shift in the pose also allowed for the formation of another hydrogen bond interaction that was not observed in the initial docked pose between His183 and carbonyl oxygen of the amide linker, however, low stability of this interaction was observed with persistence between 26% and 37%. (**Table S2, Supplement and Figures 14 and 15**).

The longer molecular dynamics simulation could confirm the stability of the obtained pose of the hit in the HDAC11 AlphaFold model in a long time scale. Inspecting the RMSD plot of the ligand showed that it is stabilizing between 4 Å and 5 Å (**Figure 11A**) with the RMSF indicating that the most fluctuating substructure is the phenoxymethyl group (**Figure 11B**).

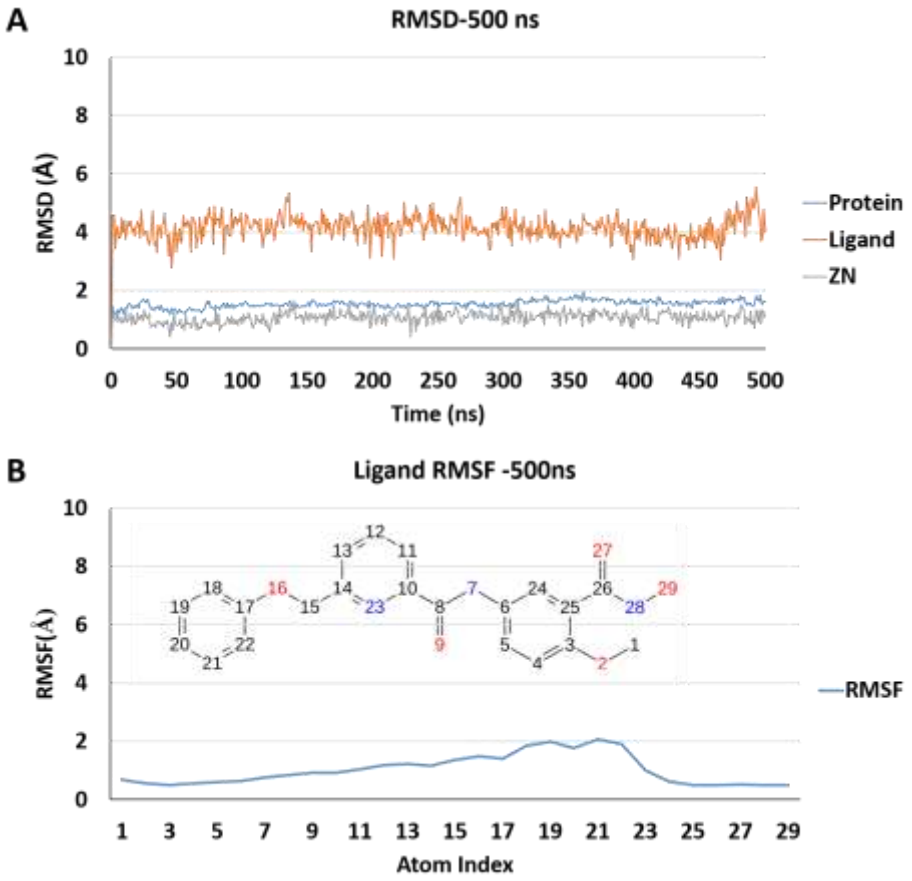

Figure 11. (**A**) RMSD plots of the protein backbone heavy atoms, zinc ion and ligand heavy atoms for the long MD run (500 ns). (**B**) RMSF plots of the ligand, ZINC000028464438 (**9**) heavy atom for the long MD run (500 ns).

Distances between the zinc ion and the chelator atoms of the hydroxamate zinc binding group showed to be stable thus confirming the bidentate chelation mode (**Figures 12A and 12B**).

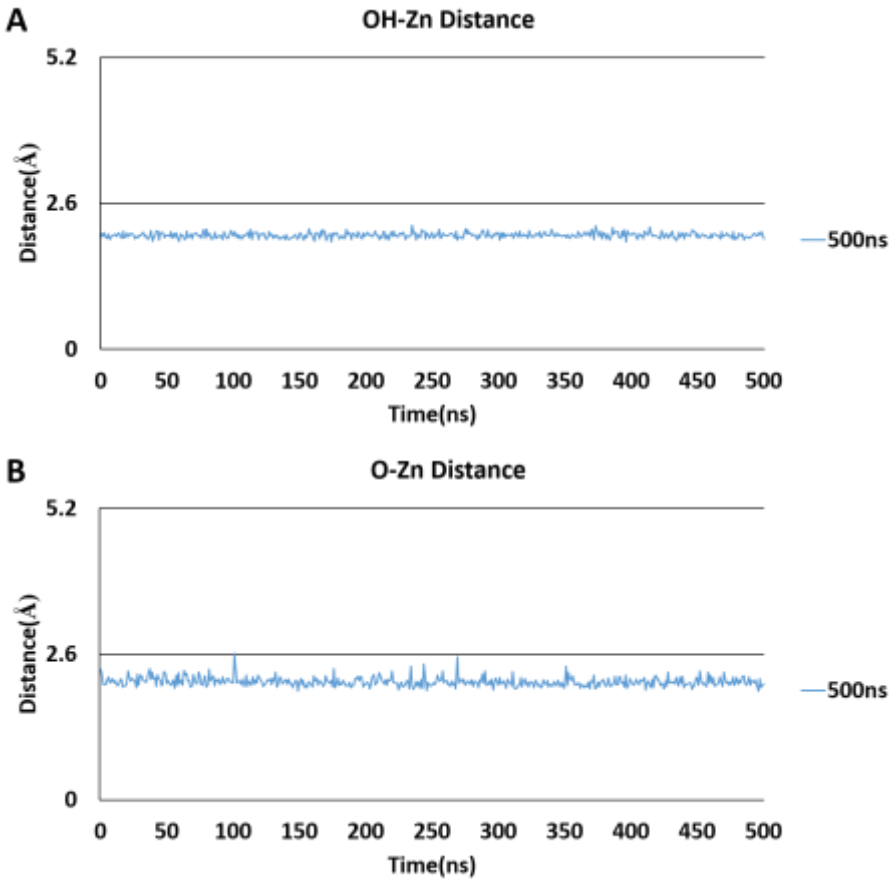

Figure 12. (**A**) and (**B**) Distances to the zinc ion for the hydroxyl and the carbonyl oxygen atoms of the hydroxamate zinc binding group, respectively, for the long MD run (500 ns).

MD simulation trajectory analysis demonstrated the same slight shift in the pose with the benzohydroxamate moiety inserted deeper into the binding pocket along with the relaxation of the phenoxymethyl capping group (**Figure 13**) as observed in the three independent shorter MD runs.

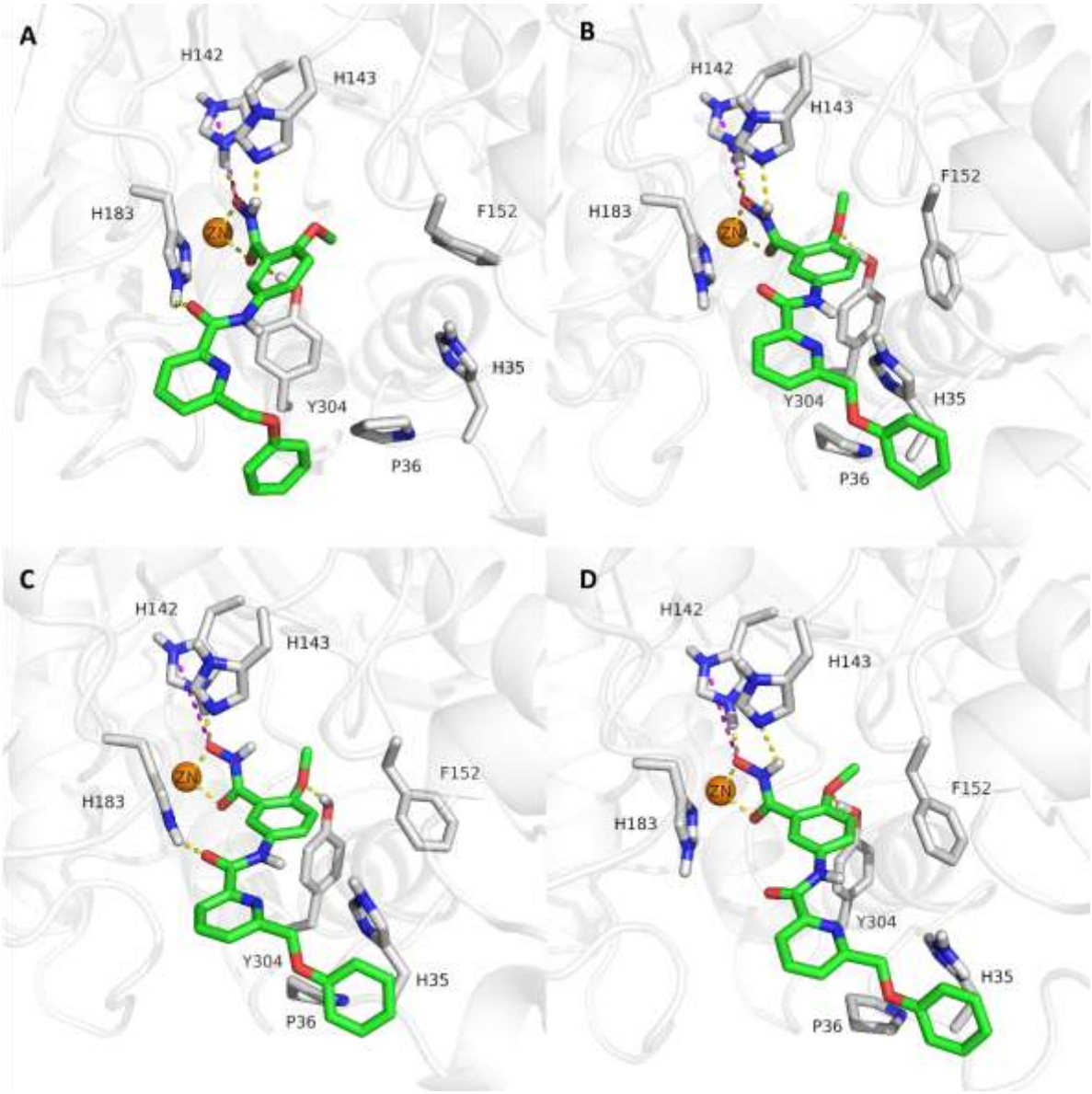

Figure 13. Selected snapshots from the long MD simulation (500 ns) of ZINC000028464438 (**9**)-HDAC11 docked pose showing the shift in the pose and fluctuation of the phenoxymethyl capping group. (**A**) Frame 1. (**B**) Frame 1250. (**C**) Frame 2500. (**D**) Frame 5000. The protein backbone is shown as white cartoon, zinc ion as orange sphere, the binding site residues as grey sticks and the ligands as green sticks. Coordination and hydrogen bonds are shown as yellow dashed lines and the ionic interactions as magenta dashed lines.

The salt bridge between the deprotonated hydroxyl oxygen of the zinc binding group and His142 showed very high stability with persistence of about 100% while for His143 the hydrogen bond interaction with the carbonyl oxygen of the hydroxamate moiety showed to be of average stability with persistence of 68%. Same observations about the other hydrogen bond interactions during the simulation in the short runs could be made. The hydrogen bond interaction between the oxygen of the methoxy group in the ortho position to the hydroxamate moiety and Tyr304 demonstrated persistence of 85%, while for His183, a weakly stable hydrogen bond with the carbonyl of the amide linker showing persistence of 42% could be observed. Overall, the predicted binding mode of the hit compound demonstrated good stability during the MD simulation. The key interactions of the zinc binding group were not affected by the slight shift of the ligand from the initial docked pose or the fluctuation of the capping group (**Figures 14 and 15)**.

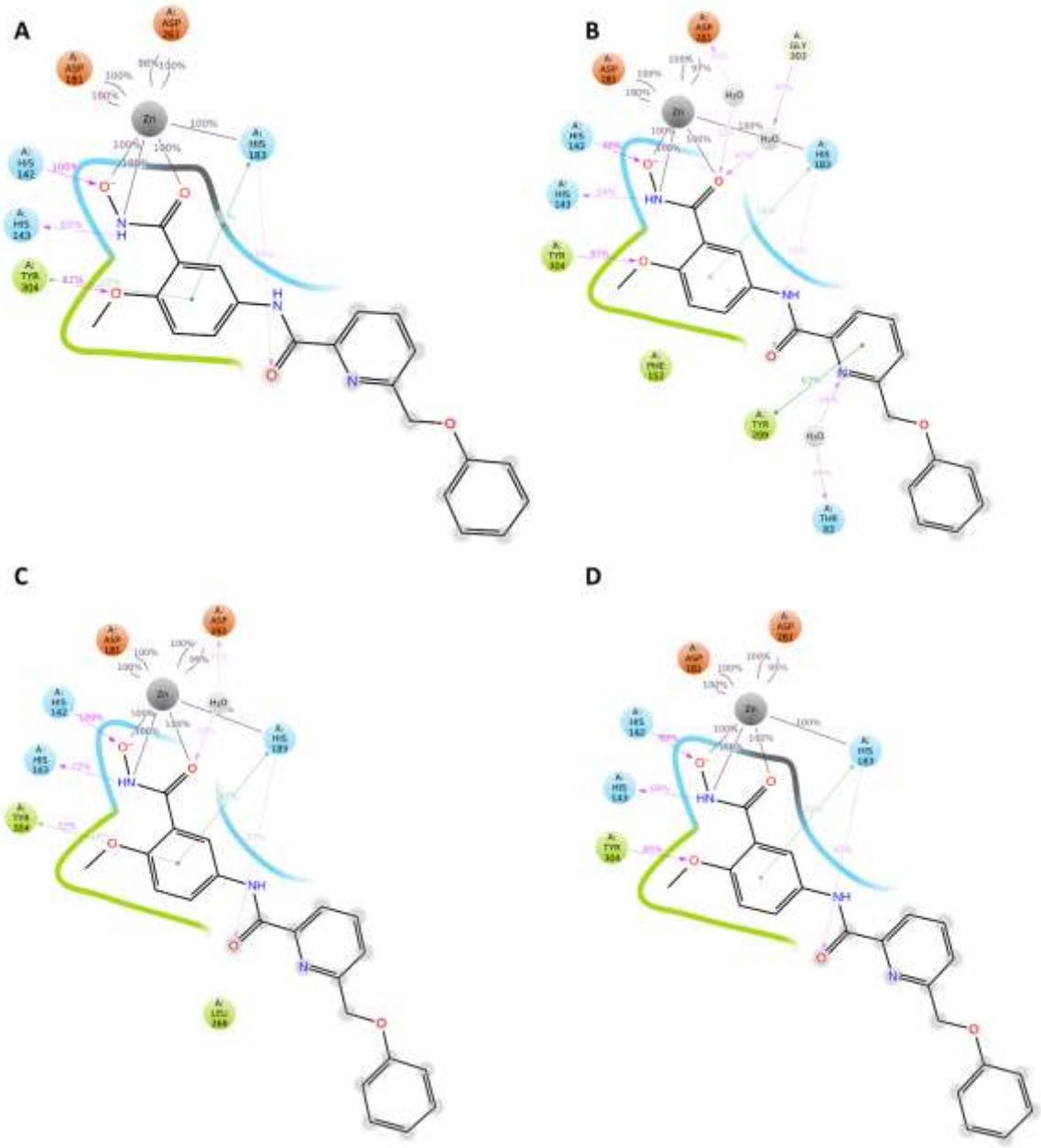

Figure 14. (**A**), (**B**), (**C**) and (**D**). Ligand interaction persistence diagram for the three independent short MD runs (50 ns) and the long MD run (500 ns), respectively of HDAC11- ZINC000028464438 (**9**).

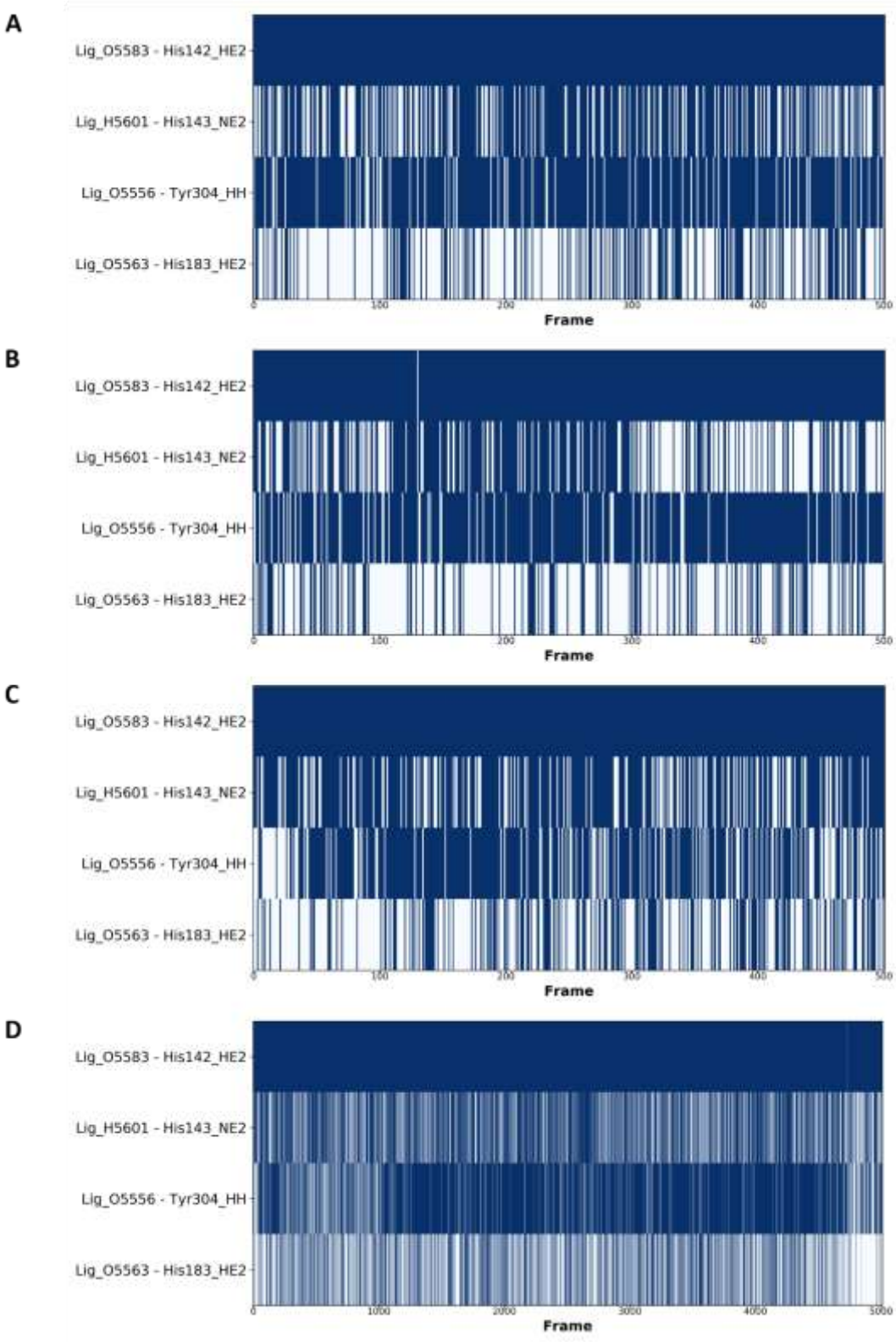

Figure 15. (**A**), (**B**), (**C**) and (**D**). Hydrogen bond occupancy diagrams for the three independent short MD runs (50 ns) and the long MD run (500 ns), respectively of HDAC11- ZINC000028464438 (**9**).

Metadynamics is an enhanced sampling technique that is able to capture the structural dynamics more efficiently in limited time scale by using a history dependent bias potential as a function of a collective variable [57]. This process helps the system escaping energy minima and previously sampled regions thus accelerating sampling of the entire complex free energy landscape.

Binding Pose Metadynamics (BPMD) application [58] implemented in Schrödinger is originally developed to rank docking poses of a single ligand in a single protein binding site by running series of metadynamics simulations. We utilized this methodology to further explore the stability of the predicted binding mode observed for the hit compound in the HDAC11 AlphaFold model.

For this purpose and as we observed a slight shift in the original docked pose during the classical MD simulation we applied the BPMD for the obtained docked pose and the last frame (500 ns) of the classical MD simulation representing the equilibrated ligand pose.

BPMD method employs the RMSD of the ligand from its initial pose as collective variable. The stability of the protein ligand complex is evaluated in terms of the ligand RMSD fluctuations and the persistence of important contacts between the ligand and the receptor over the course of the simulation. PoseScore indicates the average RMSD of the ligand, persistence score (PersScore) indicates for the persistence of the interactions over the course of the simulation and the composite score (CompScore) combines the PoseScore and PersScore [58,59].

The results from BPMD demonstrated a PoseScore of 3.226 and 1.747 for the original docked pose and the MD last frame, respectively (**Figure 16**). Generally, ligand poses with a PoseScore ≤ 2 Å were considered stable [58]. The resulted PoseScore indicates that the stabilized pose during the MD simulation is more stable when compared to the starting docked pose thus reinforcing the results obtained from the classical MD simulation which showed a slight shift of the ligand during the run.

The resulting persistence of the interactions are almost equivalent for both poses and showed a PersScore of 0.712 and 0.679 for the original docked pose and the last MD frame pose, respectively. The results are matching the defined threshold of ≥ 0.6 [58] indicating that the contact network was maintained during the course of the simulation. The CompScore for the original pose and the last frame pose of the hit ligand were found to be -0.335 and -1.647, respectively with more negative values indicating better stability.

Overall, the results from the metadynamics studies confirmed the stability of the predicted binding pose in terms of the ligand RMSD and persistence of the observed interactions and were further supporting the results from the classical MD simulations.

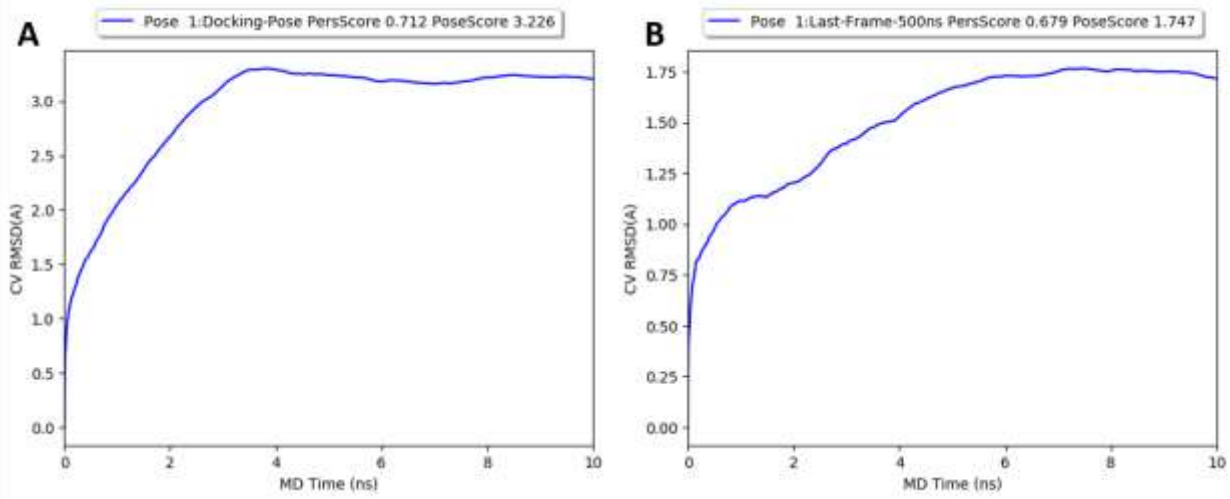

Figure 16. Plots of the average value of the collective variable (RMSD) over the metadynamics simulation. (**A**) and (**B**). The original docked pose and the pose from last frame of the 500 ns MD simulation, respectively of HDAC11-ZINC000028464438 (**9**).

3. Materials and Methods

Schrödinger Suite 2019 was used for all of the modeling work. Maestro [60] was utilized for visualization.

All ligands were docked in the deprotonated hydroxamate form while the grids for docking were all generated with the His142 (HDAC11 numbering) in the protonated HIP form. According to our experience from our previous study [32] this methodology shows better performance with the used docking software Glide in terms of reproducing the bidentate chelation native poses of the cocrystallized ligands.

3.1. Protein preparation:

All protein structures were preprocessed using Protein Preparation Wizard [61,62] by adding hydrogen atoms and assigning bond orders. Water molecules beyond 5 Å from the ligands were deleted and zero order bonds to metals were added. Filling in missing side chains and loops using Prime [63-65] was performed. Ionization states of the ligands were generated using Epik [66-68] at pH 7.0 ± 2.0. The deprotonated hydroxamates form [32,69-72] was selected for further hydrogen bond optimization. Hydrogen bond optimization was assigned with sampling water orientation and using PROPKA at pH 7.0.

3.2. Grid generation:

For all protein-ligand complexes, grids were generated using the Receptor Grid Generation panel and utilizing the centroid of the ligand as the center of the grid.

3.3. Ligand preparation:

Ligands were prepared in the predominant form at pH 7 utilizing the LigPrep [73] panel with OPLS3e force fields.

3.4. Data base acquiring and curation:

3.4.1. Acquiring ligand database:

A focused library of benzohydroxamic acids (SMARTS= C1=CC=C(C(=O)NO)C=C1) comprising 407834 ligands was downloaded from https://tldr.docking.org/ using the zinc20-all database [49].

3.4.2. Ligand preparation:

The library was prepared using Ligprep and resulted in 510529 structures using OPLS2005 [74-77] with generating possible states at pH 7.2 ± 2 using Epik. Specified chiralities from the original dataset were retained.

3.4.3. Properties calculation:

The rule of five property was calculated for all ligands in the database using QikProp [78] properties from the Molecular Descriptor panel.

3.4.4. Database filtering:

The prepared library was filtered to select the hydroxamate form [32,69-72] of the ligands using a defined custom pattern of [O-]N([H])C(=O)c1ccccc1. The library was filtered using the calculated rule of five property thereby discarding all structures which showed one or more violations for the rule of five using the Ligand Filtering panel. 18113 compounds could successfully pass the aforementioned filters.

3.5. Virtual screening:

3.5.1. Structure based pharmacophore modeling:

3.5.1.1. Pharmacophore generation:

The E-pharmacophore [79,80] hypothesis was generated using the Develop Pharmacophore Model panel form Schrödinger Phase [81-83] utilizing the optimized AlphaFold TSA-HDAC11 complex with the flipped-out Phe152 rotamer [32]. The auto E-pharmacophore method was used to specify the maximum number of features to be generated and assign the receptor-based excluded volume shell.

3.5.1.2. Pharmacophore screening:

The prepared database was screened through Phase Ligand Screening panel using the previously generated E-pharmacophore and implementing the four obtained features and excluded volumes. Up to 50 conformers were generated during the search and specifying to report at most one hit per ligand. 12154 hits could successfully pass the pharmacophore screening.

3.5.2. Docking into HDAC11 AlphaFold model:

The hits obtained from the pharmacophore screening were docked into the HDAC11 AlphaFold model using Glide [84-87] with standard precision and flexible ligand sampling. 15 poses were subjected to post docking minimization and reporting the top scored pose. 12151 compounds could be successfully docked.

Isoform	PDB ID	Resolution	Organism	Bound inhibitor
HDAC1	5ICN	3.30 Å	Homo sapiens	Hydroxamic acid inhibitor
HDAC6	5EDU	2.79 Å	Homo sapiens CD2	Hydroxamic acid inhibitor
HDAC8	5FCW	1.98 Å	Homo sapiens	Hydroxamic acid inhibitor

3.5.3. Pose filtering:

The obtained docking poses in the HDAC11 AlphaFold model were filtered using Pose Filter panel utilizing the distance between the carbonyl and the hydroxyl oxygens of the hydroxamate moiety and the zinc ion while specifying contact maximum distance to be 2.6 Å. 11409 poses could successfully pass the filter.

3.5.4. Docking and pose filtering in other HDACs isoforms:

The following crystal structures were used for the docking studies into other HDAC subtypes:

3.5.4.1. Validation by re-docking of the native ligand:

To validate the docking protocol, re-docking of the co-crystallized ligands of HDAC1 , HDAC6 and HDAC8 was performed and RMSD for the docked and the native poses was calculated. RMSD was found to be 2.018 Å, 1.192 Å and 0.416 Å for HDAC1, HDAC6 and HDAC8 respectively.

3.5.4.2. Docking and pose filtering:

The filtered poses from the HDAC11 docking results were further docked into HDAC1, HDAC6 and HDAC8. The obtained docking poses were further subjected to Pose Filter. Ligand docking and pose filtering were performed using the same settings as mentioned for HDAC11. 450, 9934 and 11308 hits could be successfully docked to HDAC1, HDAC6 and HDAC8 respectively. Compounds that could show correct poses and zinc chelation in HDAC1, HDAC6 and HDAC8 were removed from the final HDAC11 inhibitor hit list.

3.6. REOS filtering and MM-GBSA calculations:

To remove compounds with reactive groups that may interfere with biological evaluation, rapid elimination of swill (REOS) filter was applied using structure filter in Canvas [88-90].

To prioritize the hits for further evaluation, ligand binding energies were calculated using the molecular mechanics with generalized Born and surface area solvation (MM-GBSA). For this purpose, the Prime MM-GBSA panel was utilized with specifying the variable-dielectric generalized Born (VSGB) solvation model, sampling by minimizing all atoms using OPLS3e force field.

3.7. Molecular dynamics simulation:

The predicted binding mode of the virtual screening hit of HDAC11 was further analyzed by means of molecular dynamics simulation using program Desmond [91,92]. The HDAC11-inhibitor complex was simulated for 50 ns and the simulation was repeated three times applying different random seeds. Furthermore, a single longtime scale MD run was performed for 500 ns. The system was solvated in SPC water model using an orthorhombic box and a buffer distance of 10 Å distance between the solute structures and the simulation box boundary. The box volume was then minimized. The system was neutralized by adding chloride ions that were placed 4 Å away from the ligand.

Relaxation of the prepared system was performed using the default Desmond relaxation protocol for NPT ensemble followed by a production run utilizing the NPT ensemble at 300 K using a Nose–Hoover chain thermostat and a pressure of 1.01325 bar using Martyna-Tobias-Klein barostat.

The Simulation Event Analysis panel was utilized for the calculation of RMSD and distance to the zinc ion. The RMSD of the protein was calculated using the backbone atoms while the RMSD of the ligand and the zinc ion was calculated by fitting to the protein backbone. The Simulation Interaction Diagram panel was used

for analyzing the RMSF and the interaction persistence of the ligands. RMSD of the protein was calculated excluding the termini (residues: 1-14 and 321-347).

Metadynamics (implemented in the Schrödinger software) was used to assess the stability of the original docked pose compared to the stabilized pose resulting from the 500 ns MD run. For this purpose Binding Pose Metadynamics panel was utilized with the default settings of 10 trials per pose each of 10 ns. Binding Pose Metadynamics (BPMD) application [53] implemented in Schrödinger is originally developed to rank docking poses of a single ligand in a single protein binding site by running series of metadynamics simulations. We utilized this methodology to further explore the stability of the predicted binding modes.

3.8. Chemistry:

3.8.1. General

Materials and reagents were purchased from Sigma-Aldrich Co. Ltd (St. Louis, MI, USA) and abcr GmbH (Karlsruhe, Germany). Solvents used during the synthesis and purification were analytically pure and dry. Thin layer chromatography was carried out using aluminum sheets coated with silica gel 60 F254 (Merck, Darmstadt, Germany). For medium pressure chromatography (MPLC), columns containing silica gel Biotage® (Biotage, Uppsala, Sweden) SNAP ultra-HP-sphere 25 µm, were used.

The purity of the hit compound was determined using high-pressure liquid chromatography (HPLC) and was measured by UV absorbance at 254 nm. The HPLC system consisted of two LC-10AD pumps, a SPD-M10A VP PDA detector, and a SIL-HT autosampler, from the manufacturer Shimadzu (Kyoto, Japan). For the stationary phase, Merck LiChrospher 100 RP18, 125 mm x 4 mm, 5 µm column was used. The mobile phase was composed of was Methanol, H_2O, and 0.05% trifluroacetic acid.

Mass spectrometry (MS) analyses was carried out on a Finnigan MAT710C (Thermo Separation Products) for the ESI MS spectra. High-resolution mass spectrometry (HRMS-ESI) analyses was performed with a LTQ (linear ion trap) Orbitrap XL hybrid mass spectrometer (Thermo FisherScientific). ^{1}HNMR and ^{13}CNMR spectra were taken on a Varian Inova 400using using deuterated dimethyl sulfoxide (DMSO-d6) as solvent. Chemical shifts were referenced to the residual solvent signals

The hit compound was synthesized according to **Scheme 1**.

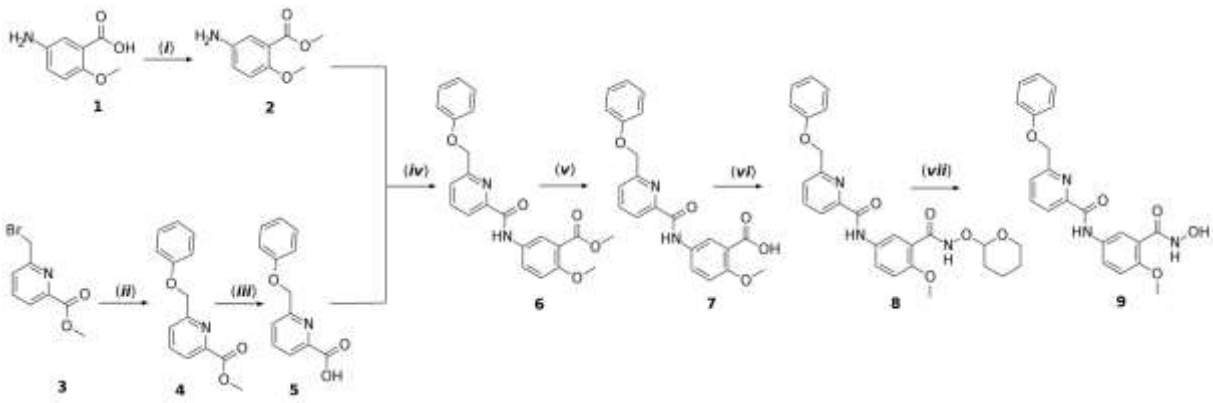

Scheme 1. Synthesis of target compound. **Reagents and conditions:** (*i*) - $SOCl_2$ / methanol / reflux /3 h; (*ii*) - C_6H_6OH / Cs_2CO_3 / DMF / RT / 18 h; (*iii*) - $LiOH.H_2O$ / THF:H_2O (50:50) / RT / 1h; (*iv*) **5** / $C_2O_2Cl_2$ / DCM / RT /2h then **2** / DIPEA / RT / overnight; (*v*) - $LiOH.H_2O$ / THF:H_2O (50:50) / RT / 4h; (*vi*) - O-(Tetrahydro-2H-pyran-2-yl)-hydroxylamin / HATU / DIPEA / DMF / RT / 4 h; (*vii*) – THF / aq. HCl / RT / overnight.

3.8.2. Synthesis procedure:

Methyl 5-amino-2-methoxybenzoate hydrochloride **(2)**.

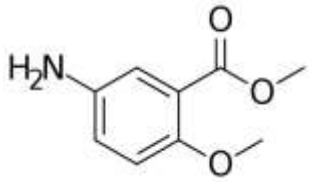

To a stirred solution of 5-amino-2-methoxybenzoic acid **1** (0.5 g, 3 mmol) in methanol, thionyl chloride, (0.33 mL, 4.5 mmol), was added dropwise. The mixture was heated under reflux for 3 hours and then cooled and evaporated using rotary evaporator to afford the product as hydrochloride salt. ^{1}H NMR (400 MHz, DMSO-d$_6$) δ 10.29 (s, 3H), 7.64 (d, *J* = 2.8 Hz, 1H), 7.53 (dd, *J* = 8.9, 2.8 Hz, 1H), 7.24 (d, *J* = 9.0 Hz, 1H), 3.81 (s, 3H), 3.78 (s, 3H). MS m/z: [M + H]$^+$ 182, Yield, 98.31%.

Methyl 6-(phenoxymethyl)pyridine-2-carboxylate (**4**).

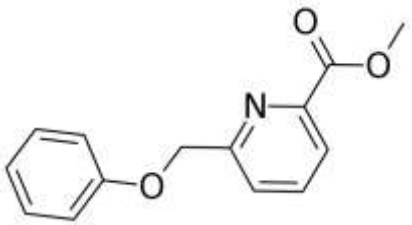

A mixture of methyl 6-(bromomethyl) picolinate **3** (1.38 g, 6 mmol), phenol (0.71 g, 7.5 mmol) and cesium carbonate (2.94 g, 9 mmol) in 20 mL DMF was stirred at room temperature for 18 hours. The reaction mixture then was added dropwise to iced water and the formed precipitate was filtered and washed with water. ^{1}H NMR (400 MHz, DMSO-d$_6$) δ 8.06 – 7.95 (m, 2H), 7.77 – 7.70 (m, 1H), 7.33 – 7.23 (m, 2H), 7.06 – 6.97 (m, 2H), 6.97 – 6.88 (m, 1H), 5.22 (s, 2H), 3.87 (s, 3H). MS m/z: [M + H]$^+$ 244, Yield, 82.92%.

6-(phenoxymethyl)pyridine-2-carboxylic acid (**5**).

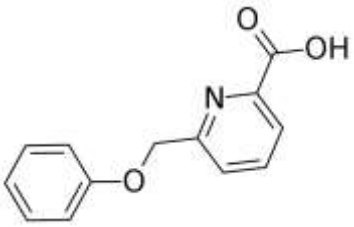

A mixture of **4** (1.21 g, 5 mmol) and lithium hydroxide monohydrate (1.05 g, 25 mmol) was stirred in a mixture of water and tetrahydrofuran (50:50) for one hour at room temperature. The reaction mixture then was added dropwise to iced water and neutralized by adding acetic acid. The mixture was then extracted with ethyl acetate and the organic layer was dried over anhydrous sodium sulfate and evaporated using rotary evaporator to afford the solid product. ^{1}H NMR (400 MHz, DMSO-d$_6$) δ 13.20 (s, 1H), 8.03 – 7.93 (m, 2H), 7.71 (dd, *J* = 7.1, 1.8 Hz, 1H), 7.33 – 7.24 (m, 2H), 7.07 – 6.98 (m, 2H), 6.97 – 6.90 (m, 1H), 5.21 (s, 2H). MS m/z: [M + H]$^+$ 230, Yield, 92.09%.

Methyl 2-methoxy-5-[6-(phenoxymethyl)pyridine-2-amido]benzoate (**6**).

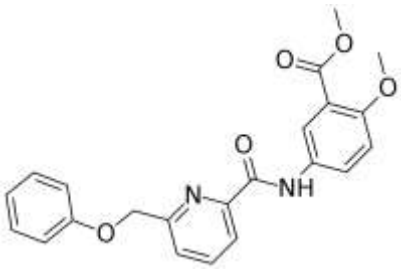

To a stirred solution of **5**, (0.55 g, 2.4 mmol) in DCM, oxalyl chloride (0.26 mL, 3mmol) was added dropwise and the mixture was stirred for 3 hours at room temperature. The mixture was then added dropwise to a

solution of (0.52 g, 2.4 mmol) of **2** and N,N-diisopropylethylamine (DIPEA) (1.09 g, 8.4 mmol) in DCM and the mixture was stirred over night at room temperature. The reaction mixture was washed with saturated aqueous solutions of ammonium chloride and sodium carbonate followed by brine. The organic layer was then dried over anhydrous sodium sulfate and evaporated using rotary evaporator. The product was purified with medium pressure liquid chromatography (MPLC) using mixture of n-heptane and ethyl acetate. ^{1}H NMR (400 MHz, DMSO-d_6) δ 10.51 (s, 1H), 8.19 (d, *J* = 2.7 Hz, 1H), 8.09 – 8.02 (m, 2H), 8.00 (dd, *J* = 9.0, 2.8 Hz, 1H), 7.73 (dd, *J* = 6.4, 2.4 Hz, 1H), 7.34 – 7.25 (m, 2H), 7.16 (d, *J* = 9.1 Hz, 1H), 7.09 – 7.00 (m, 2H), 6.98 – 6.91 (m, 1H), 5.32 (s, 2H), 3.80 (s, 3H), 3.79 (s, 3H). MS m/z: $[M + H]^+$ 393.1, Yield, 74.35%.

2-methoxy-5-[6-(phenoxymethyl)pyridine-2-amido]benzoic acid (**7**).

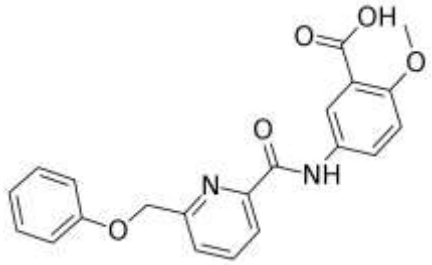

(0.68 g, 1.7 mmol) of **6** was dissolved in a mixture of tetrahydrofuran and water (50:50) and (0.355 g, 8.5 mmol) of lithium hydroxide monohydrate was added and the reaction mixture was stirred for 4 hours at room temperature. The reaction mixture was added dropwise to iced water and neutralized by acetic acid. The solution then was saturated with sodium chloride and the solid precipitate was filtered and washed with water. ^{1}H NMR (400 MHz, DMSO-d_6) δ 12.70 (s, 1H), 10.48 (s, 1H), 8.15 (d, *J* = 2.7 Hz, 1H), 8.10 – 8.01 (m, 2H), 7.96 (dd, *J* = 9.0, 2.8 Hz, 1H), 7.73 (dd, *J* = 6.8, 2.1 Hz, 1H), 7.34 – 7.26 (m, 2H), 7.12 (d, *J* = 9.0 Hz, 1H), 7.08 – 7.00 (m, 2H), 6.98 – 6.90 (m, 1H), 5.32 (s, 2H), 3.79 (s, 3H). MS m/z: $[M + H]^+$ 379,1, Yield, 94.56%

N-{4-methoxy-3-[(oxan-2-yloxy)carbamoyl]phenyl}-6-(phenoxymethyl)pyridine-2-carboxamide (**8**).

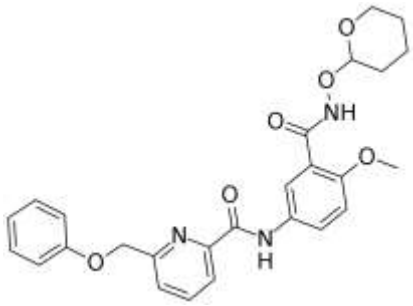

A mixture of **7**, (0.57 g, 1.5 mmol) and hexafluorophosphate azabenzotriazole tetramethyl uronium (HATU) (0.68 g, 1.8 mmol) in DMF was stirred for 15 min after which O-(tetrahydro-2H-pyran-2-yl)-hydroxylamin (0.2 g, 1.7 mmol) and DIPEA (0.58 g, 4.5 mmol) were added and stirring was continued for 4 hours. The reaction mixture was diluted with water and extracted with ethyl acetate. The organic layer was washed with saturated solutions of ammonium chloride and sodium carbonate followed by brine. The organic layer was dried over anhydrous sodium sulfate and evaporated using rotary evaporator. The product was purified using medium pressure liquid chromatography (MPLC) using a mixture on n-heptane and ethyl acetate. ^{1}H NMR (400 MHz, DMSO-d_6) δ 11.02 (s, 1H), 10.49 (s, 1H), 8.13 – 8.00 (m, 3H), 7.96 (dd, *J* = 8.9, 2.8 Hz, 1H), 7.73 (dd, *J* = 6.5, 2.3 Hz, 1H), 7.35 – 7.25 (m, 2H), 7.12 (d, *J* = 9.0 Hz, 1H), 7.08 – 7.00 (m, 2H), 6.99 – 6.91 (m, 1H), 5.32 (s, 2H), 5.06 – 4.96 (m, 1H), 4.08 – 3.97 (m, 1H), 3.82 (s, 3H), 3.55 – 3.44 (m, 1H), 1.81 – 1.62 (m, 3H), 1.60 – 1.44 (m, 3H). MS m/z: $[M + H]^+$ 478.2. Yield, 84.8%

N-[3-(hydroxycarbamoyl)-4-methoxyphenyl]-6-(phenoxymethyl)pyridine-2-carboxamide (**9**).

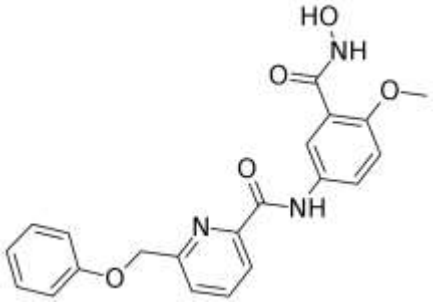

(0.58 g, 1.2 mmol) of **8** was dissolved in 20 mL of tetrahydrofuran and 1 mL of 2N aqueous HCl was added and the mixture was stirred overnight. The reaction mixture was then added dropwise to iced water and the precipitate was filtered and washed with water. ^{1}H NMR (400 MHz, DMSO-d_6) δ 10.62 (s, 1H), 10.47 (s, 1H), 9.09 (s, 1H), 8.13 – 8.00 (m, 3H), 7.93 (dd, *J* = 9.0, 2.8 Hz, 1H), 7.73 (dd, *J* = 6.6, 2.2 Hz, 1H), 7.36 – 7.25 (m, 2H), 7.11 (d, *J* = 9.0 Hz, 1H), 7.08 – 7.00 (m, 2H), 6.99 – 6.90 (m, 1H), 5.32 (s, 2H), 3.82 (s, 3H). ^{13}C NMR (101 MHz, DMSO-d_6) δ 163.15, 162.49, 158.44, 156.55, 153.46, 149.75, 139.36, 131.68, 130.07, 124.98, 124.01, 122.77, 122.53, 121.65, 121.52, 115.20, 112.48, 70.13, 56.35. MS m/z: $[M + H]^+$ 394.3, HRMS m/z: $[M + H]^+$ 394.1394; calculated $C_{21}H_{20}O_5N_3$: 394.1403. HPLC: rt 13.123 min (purity 95.755%), Yield 77.43%.

3.9. In vitro enzymatic inhibition evaluation:

In case of HDAC11 the full-length human was expressed and purified as described in previous work [22]. A fluorescence based HDAC11 assay was used. The fluorescence measurements were performed using a PerkinElmer Envision 2104 multilabel plate reader (Waltham, MA, USA) at λex = 320 nm and λem = 430 nm. The reaction mixture consisted of HDAC11, and the fatty acid acylated peptide substrate derived from TNFα in a reaction buffer comprising 50 mM HEPES, 2 mg/mL BSA, and 70 μMTCEP, and at pH 7.4 which was adjusted with NaOH (total volume 40 μL). The reactions were incubated in black 384-well plates for 30 min (scan every 30 s) at room temperature, and the increase of relative fluorescence reflecting the product formation was monitored. Positive (HDAC11, substrate, DMSO and buffer) and negative controls (substrate, DMSO and Buffer) were included in every measurement. They were set as 100 and 0 % respectively and the measured values were normalized accordingly.

For HDAC1, 2, 3, 6 and HDAC6 the recombinant proteins were purchased from ENZO Life Sciences AG (Lausen, CH) whereas HDAC4 - 7, 9 and 10 were produced as described in previous work [93]. All inhibitors were tested in an enzymatic in vitro assay as described before using 384-well plates (GreinerONe, catalogue no. 784900) [55,93]. After five minutes of incubation of inhibitors with the respective enzyme (HDAC1: 10 nM, HDAC2 and 3: 3 nM, HDAC4: 5 nM, HDAC5: 10 nM, HDAC6: 1 nM, HDAC7: 5 nM, HDAC8: 2 nM, HDAC 9: 20 nM, HDAC10: 5 nM), the reactions were started by the addition of the substrate.

For HDAC1, 2, 3 and 6, an acetylated peptide substrate derived from p53 (Ac-RHKK(Acetyl)-AMC) was used in a discontinuous fluorescence assay. as described before [55]. All reactions were performed in assay buffer (20 mM HEPES, 140 mM NaCl, 10 mM MgCl2, 1 mM TCEP and 0.2 mg/mL BSA, pH 7.4 adjusted with NaOH) at 37 °C. After 1 hour the reaction was quenched by adding trypsin and SAHA. The fluorescence inten-sity was measured after 1 hour of incubation using an Envision 2104 Multilabel Plate Reader (PerkinElmer, Waltham, MA), with an excitation wavelength of 380 ± 8 nm and an emission wavelength of 430 ± 8 nm.

HDAC4 – 7, 8, 9 and 10 were measured in a continuous manner using the thioacety-lated peptide substrate (Abz-SRGGK(thio-TFA)FFRR-NH2), which was described before [93]. For HDAC 10, an internal quenched spermidine-like substrate was used. The fluorescence increase was followed for 1 hour with two reads per min with an excitation wavelength of 320 ± 8 nm and an emission wavelength of 430 ± 8 nm. For all measure-ments, positive (enzyme, substrate, DMSO and buffer) and negative (substrate, DMSO and Buffer) controls were included in every measurement and were set as 100 and 0 %, respec-tively. The measured values were normalized accordingly.

4. Conclusions

In the current study a structure-based pharmacophore model utilizing our previously optimized HDAC11 AlphaFold model was implemented as preliminary step for screening a large, focused library of benzohydroxamate compounds. The resulted hits were further docked in HDAC11 model and followed by pose filtration

to select compounds that could show bidentate chelation of the catalytic zinc ion. A comparative approach was then applied by screening the hits obtained from docking in HDAC11 using different selected HDAC isoform (HDAC1, HDAC6 and HDAC8) crystal structures and eliminating compounds that showed good poses in other HDAC isoforms. This approach proved effective in filtering the initially obtained hit compounds to find a selective ligand. The obtained hits that could show good poses in HDAC11 but not in the other isoforms were subjected to a final filtration step using REOS filter and the final hits were further prioritized by MM-GBSA calculations. It is interesting to see that all top-ranked hits have a substituent in ortho-position to the aromatic hydroxamate group. This ortho-substituent is sterically accepted in the HDAC11 binding pocket only. In all other HDAC structures studied in the current work this substitution leads to the abolition of the correct chelation of the zinc ion. The experimentally confirmed selectivity for HDAC11 underpins the usefulness of the optimized HDAC11 AlphaFold model for structure-based drug design.

Moreover, the binding mode of the confirmed hit in HDAC11 was further analyzed by several MD simulations. MD simulation studies proved the stability of the initially observed binding mode in terms of ligand RMSD, RMSF, bidentate chelation of the zinc ion and interaction stability.

As a conclusion, a multistep and comparative virtual screening approach was successfully implemented in an attempt to identify novel selective HDAC11 inhibitors utilizing a previously optimized HDAC11 AlphaFold model. This study verifies experimentally the HDAC11 AlphaFold model optimization approach we adopted in our previous study. Additionally, it also confirms that AlphaFold models can be utilized for the aim of drug design and discovery subsequent to a prior optimization.

Supplementary Materials: The following supporting information are available: Details on the chemical synthesis and analytical characterization as well as details on the hit selection process.

Author Contributions: FB did the computational studies, synthesized the compound and wrote the manuscript. D. R. supervised the computational studies and wrote part of the manuscript. M. Z. performed the HDAC in vitro testing of the hit compound. C.B. expressed the HDAC11 protein for in vitro testing. M.S. and WS supervised the experiments and revised the manuscript.

Funding: This study was supported by the Deutsche Forschungsgemeinschaft (DFG) grants 469954457 and 471614207. This work was in part supported by the CAS (RVO: 86652036) and the Grant Agency of the Czech Republic (24-12155S) (C.B.).

Conflicts of Interest: The authors declare no conflict of interest.

References

1. Lombardi, P.M.; Cole, K.E.; Dowling, D.P.; Christianson, D.W. Structure, mechanism, and inhibition of histone deacetylases and related metalloenzymes. *Curr Opin Struct Biol* **2011**, *21*, 735-743, doi:10.1016/j.sbi.2011.08.004.

2. Marek, M.; Shaik, T.B.; Romier, C. Structural Biology of Epigenetic Targets: Exploiting Complexity. In *Epigenetic Drug Discovery*; Methods and Principles in Medicinal Chemistry; 2019; pp. 11-44.

3. Liu, S.-S.; Wu, F.; Jin, Y.-M.; Chang, W.-Q.; Xu, T.-M. HDAC11: a rising star in epigenetics. *Biomedicine & Pharmacotherapy* **2020**, *131*, 110607, doi:https://doi.org/10.1016/j.biopha.2020.110607.

4. Gao, L.; Cueto, M.A.; Asselbergs, F.; Atadja, P. Cloning and functional characterization of HDAC11, a novel member of the human histone deacetylase family. *J Biol Chem* **2002**, *277*, 25748-25755, doi:10.1074/jbc.M111871200.

5. Boltz, T.A.; Khuri, S.; Wuchty, S. Promoter conservation in HDACs points to functional implications. *BMC Genomics* **2019**, *20*, 613, doi:10.1186/s12864-019-5973-x.

6. Yanginlar, C.; Logie, C. HDAC11 is a regulator of diverse immune functions. *Biochimica et Biophysica Acta (BBA) - Gene Regulatory Mechanisms* **2018**, *1861*, 54-59, doi:https://doi.org/10.1016/j.bbagrm.2017.12.002.

7. Villagra, A.; Cheng, F.; Wang, H.W.; Suarez, I.; Glozak, M.; Maurin, M.; Nguyen, D.; Wright, K.L.; Atadja, P.W.; Bhalla, K.; et al. The histone deacetylase HDAC11 regulates the expression of interleukin 10 and immune tolerance. *Nat Immunol* **2009**, *10*, 92-100, doi:10.1038/ni.1673.

8. Glozak, M.A.; Seto, E. Acetylation/deacetylation modulates the stability of DNA replication licensing factor Cdt1. *J Biol Chem* **2009**, *284*, 11446-11453, doi:10.1074/jbc.M809394200.

9. Cao, J.; Sun, L.; Aramsangtienchai, P.; Spiegelman, N.A.; Zhang, X.; Huang, W.; Seto, E.; Lin, H. HDAC11 regulates type I interferon signaling through defatty-acylation of SHMT2. *Proc Natl Acad Sci U S A* **2019**, *116*, 5487-5492, doi:10.1073/pnas.1815365116.

10. Bagchi, R.A.; Ferguson, B.S.; Stratton, M.S.; Hu, T.; Cavasin, M.A.; Sun, L.; Lin, Y.H.; Liu, D.; Londono, P.; Song, K.; et al. HDAC11 suppresses the thermogenic program of adipose tissue via BRD2. *JCI Insight* **2018**, *3*, doi:10.1172/jci.insight.120159.

11. Sun, L.; Marin de Evsikova, C.; Bian, K.; Achille, A.; Telles, E.; Pei, H.; Seto, E. Programming and Regulation of Metabolic Homeostasis by HDAC11. *EBioMedicine* **2018**, *33*, 157-168, doi:10.1016/j.ebiom.2018.06.025.

12. Fei, Q.; Song, F.; Jiang, X.; Hong, H.; Xu, X.; Jin, Z.; Zhu, X.; Dai, B.; Yang, J.; Sui, C.; et al. LncRNA ST8SIA6-AS1 promotes hepatocellular carcinoma cell proliferation and resistance to apoptosis by targeting miR-4656/HDAC11 axis. *Cancer Cell Int* **2020**, *20*, 232, doi:10.1186/s12935-020-01325-5.

13. Freese, K.; Seitz, T.; Dietrich, P.; Lee, S.M.L.; Thasler, W.E.; Bosserhoff, A.; Hellerbrand, C. Histone Deacetylase Expressions in Hepatocellular Carcinoma and Functional Effects of Histone Deacetylase Inhibitors on Liver Cancer Cells In Vitro. *Cancers (Basel)* **2019**, *11*, doi:10.3390/cancers11101587.

14. Gong, D.; Zeng, Z.; Yi, F.; Wu, J. Inhibition of histone deacetylase 11 promotes human liver cancer cell apoptosis. *Am J Transl Res* **2019**, *11*, 983-990.

15. Huo, W.; Qi, F.; Wang, K. Long non-coding RNA BCYRN1 promotes prostate cancer progression via elevation of HDAC11. *Oncol Rep* **2020**, *44*, 1233-1245, doi:10.3892/or.2020.7680.

16. Wang, W.; Ding, B.; Lou, W.; Lin, S. Promoter Hypomethylation and miR-145-5p Downregulation- Mediated HDAC11 Overexpression Promotes Sorafenib Resistance and Metastasis of Hepatocellular Carcinoma Cells. *Front Cell Dev Biol* **2020**, *8*, 724, doi:10.3389/fcell.2020.00724.

17. Wang, W.; Fu, L.; Li, S.; Xu, Z.; Li, X. Histone deacetylase 11 suppresses p53 expression in pituitary tumor cells. *Cell Biol Int* **2017**, *41*, 1290-1295, doi:10.1002/cbin.10834.

18. Mithraprabhu, S.; Kalff, A.; Chow, A.; Khong, T.; Spencer, A. Dysregulated Class I histone deacetylases are indicators of poor prognosis in multiple myeloma. *Epigenetics* **2014**, *9*, 1511-1520, doi:10.4161/15592294.2014.983367.

19. Yue, L.; Sharma, V.; Horvat, N.P.; Akuffo, A.A.; Beatty, M.S.; Murdun, C.; Colin, C.; Billington, J.M.R.; Goodheart, W.E.; Sahakian, E.; et al. HDAC11 deficiency disrupts oncogene-induced hematopoiesis in myeloproliferative neoplasms. *Blood* **2020**, *135*, 191-207, doi:10.1182/blood.2019895326.

20. Thole, T.M.; Lodrini, M.; Fabian, J.; Wuenschel, J.; Pfeil, S.; Hielscher, T.; Kopp-Schneider, A.; Heinicke, U.; Fulda, S.; Witt, O.; et al. Neuroblastoma cells depend on HDAC11 for mitotic cell cycle progression and survival. *Cell Death Dis* **2017**, *8*, e2635, doi:10.1038/cddis.2017.49.

21. Kutil, Z.; Mikešová, J.; Zessin, M.; Meleshin, M.; Nováková, Z.; Alquicer, G.; Kozikowski, A.; Sippl, W.; Bařinka, C.; Schutkowski, M. Continuous Activity Assay for HDAC11 Enabling Reevaluation of HDAC Inhibitors. *ACS Omega* **2019**, *4*, 19895-19904, doi:10.1021/acsomega.9b02808.

22. Kutil, Z.; Novakova, Z.; Meleshin, M.; Mikesova, J.; Schutkowski, M.; Barinka, C. Histone Deacetylase 11 Is a Fatty-Acid Deacylase. *ACS Chemical Biology* **2018**, *13*, 685-693, doi:10.1021/acschembio.7b00942.

23. Moreno-Yruela, C.; Galleano, I.; Madsen, A.S.; Olsen, C.A. Histone Deacetylase 11 Is an ε-N-Myristoyllysine Hydrolase. *Cell Chemical Biology* **2018**, *25*, 849-856.e848, doi:https://doi.org/10.1016/j.chembiol.2018.04.007.

24. Martin, M.W.; Lee, J.Y.; Lancia, D.R.; Ng, P.Y.; Han, B.; Thomason, J.R.; Lynes, M.S.; Marshall, C.G.; Conti, C.; Collis, A.; et al. Discovery of novel N-hydroxy-2-arylisoindoline-4-carboxamides as potent and selective inhibitors of HDAC11. *Bioorganic & Medicinal Chemistry Letters* **2018**, *28*, 2143-2147, doi:https://doi.org/10.1016/j.bmcl.2018.05.021.

25. Dallavalle, S.; Musso, L.; Cincinelli, R.; Darwiche, N.; Gervasoni, S.; Vistoli, G.; Guglielmi, M.B.; La Porta, I.; Pizzulo, M.; Modica, E.; et al. Antitumor activity of novel POLA1-HDAC11 dual inhibitors. *European Journal of Medicinal Chemistry* **2022**, *228*, 113971, doi:https://doi.org/10.1016/j.ejmech.2021.113971.

26. Bai, P.; Liu, Y.; Yang, L.; Ding, W.; Mondal, P.; Sang, N.; Liu, G.; Lu, X.; Ho, T.T.; Zhou, Y.; et al. Development and Pharmacochemical Characterization Discover a Novel Brain-Permeable HDAC11-Selective Inhibitor with Therapeutic Potential by Regulating Neuroinflammation in Mice. *Journal of Medicinal Chemistry* **2023**, doi:10.1021/acs.jmedchem.3c01491.

27. Bora-Singhal, N.; Mohankumar, D.; Saha, B.; Colin, C.M.; Lee, J.Y.; Martin, M.W.; Zheng, X.; Coppola, D.; Chellappan, S. Novel HDAC11 inhibitors suppress lung adenocarcinoma stem cell self-renewal and overcome drug resistance by suppressing Sox2. *Scientific Reports* **2020**, *10*, 4722, doi:10.1038/s41598-020-61295-6.

28. Son, S.I.; Cao, J.; Zhu, C.L.; Miller, S.P.; Lin, H. Activity-Guided Design of HDAC11-Specific Inhibitors. *ACS Chem Biol* **2019**, *14*, 1393-1397, doi:10.1021/acschembio.9b00292.

29. Sun, P.; Wang, J.; Khan, K.S.; Yang, W.; Ng, B.W.; Ilment, N.; Zessin, M.; Bülbül, E.F.; Robaa, D.; Erdmann, F.; et al. Development of Alkylated Hydrazides as Highly Potent and Selective Class I Histone Deacetylase Inhibitors with T cell Modulatory Properties. *J Med Chem* **2022**, *65*, 16313-16337, doi:10.1021/acs.jmedchem.2c01132.

30. Pulya, S.; Himaja, A.; Paul, M.; Adhikari, N.; Banerjee, S.; Routholla, G.; Biswas, S.; Jha, T.; Ghosh, B. Selective HDAC3 Inhibitors with Potent In Vivo Antitumor Efficacy against Triple-Negative Breast Cancer. *J Med Chem* **2023**, *66*, 12033-12058, doi:10.1021/acs.jmedchem.3c00614.

31. Ho, T.T.; Peng, C.; Seto, E.; Lin, H. Trapoxin A Analogue as a Selective Nanomolar Inhibitor of HDAC11. *ACS Chem Biol* **2023**, *18*, 803-809, doi:10.1021/acschembio.2c00840.

32. Baselious, F.; Robaa, D.; Sippl, W. Utilization of AlphaFold models for drug discovery: Feasibility and challenges. Histone deacetylase 11 as a case study. *Computers in Biology and Medicine* **2023**, 107700, doi:https://doi.org/10.1016/j.compbiomed.2023.107700.

33. Jumper, J.; Evans, R.; Pritzel, A.; Green, T.; Figurnov, M.; Ronneberger, O.; Tunyasuvunakool, K.; Bates, R.; Žídek, A.; Potapenko, A.; et al. Highly accurate protein structure prediction with AlphaFold. *Nature* **2021**, *596*, 583-589, doi:10.1038/s41586-021-03819-2.

34. David, A.; Islam, S.; Tankhilevich, E.; Sternberg, M.J.E. The AlphaFold Database of Protein Structures: A Biologist's Guide. *J Mol Biol* **2022**, *434*, 167336, doi:10.1016/j.jmb.2021.167336.

35. Ren, F.; Ding, X.; Zheng, M.; Korzinkin, M.; Cai, X.; Zhu, W.; Mantsyzov, A.; Aliper, A.; Aladinskiy, V.; Cao, Z.; et al. AlphaFold accelerates artificial intelligence powered drug discovery: efficient discovery of a novel CDK20 small molecule inhibitor. *Chemical Science* **2023**, *14*, 1443-1452, doi:10.1039/D2SC05709C.

36. Zhu, W.; Liu, X.; Li, Q.; Gao, F.; Liu, T.; Chen, X.; Zhang, M.; Aliper, A.; Ren, F.; Ding, X.; et al. Discovery of novel and selective SIK2 inhibitors by the application of AlphaFold structures and generative models. *Bioorganic & Medicinal Chemistry* **2023**, *91*, 117414, doi:https://doi.org/10.1016/j.bmc.2023.117414.

37. Holcomb, M.; Chang, Y.T.; Goodsell, D.S.; Forli, S. Evaluation of AlphaFold2 structures as docking targets. *Protein Sci* **2023**, *32*, e4530, doi:10.1002/pro.4530.

38. He, X.-h.; You, C.-z.; Jiang, H.-l.; Jiang, Y.; Xu, H.E.; Cheng, X. AlphaFold2 versus experimental structures: evaluation on G protein-coupled receptors. *Acta Pharmacologica Sinica* **2023**, *44*, 1-7, doi:10.1038/s41401-022-00938-y.

39. Lee, S.; Kim, S.; Lee, G.R.; Kwon, S.; Woo, H.; Seok, C.; Park, H. Evaluating GPCR modeling and docking strategies in the era of deep learning-based protein structure prediction. *Comput Struct Biotechnol J* **2023**, *21*, 158-167, doi:10.1016/j.csbj.2022.11.057.

40. Heo, L.; Feig, M. Multi-state modeling of G-protein coupled receptors at experimental accuracy. *Proteins* **2022**, *90*, 1873-1885, doi:10.1002/prot.26382.

41. Karelina, M.; Noh, J.J.; Dror, R.O. How accurately can one predict drug binding modes using AlphaFold models? **2023**, doi:10.7554/elife.89386.1.

42. Díaz-Rovira, A.M.; Martín, H.; Beuming, T.; Díaz, L.; Guallar, V.; Ray, S.S. Are Deep Learning Structural Models Sufficiently Accurate for Virtual Screening? Application of Docking Algorithms to AlphaFold2 Predicted Structures. *Journal of Chemical Information and Modeling* **2023**, *63*, 1668-1674, doi:10.1021/acs.jcim.2c01270.

43. Scardino, V.; Di Filippo, J.I.; Cavasotto, C.N. How good are AlphaFold models for docking-based virtual screening? *iScience* **2023**, *26*, 105920, doi:10.1016/j.isci.2022.105920.

44. Zhang, Y.; Vass, M.; Shi, D.; Abualrous, E.; Chambers, J.M.; Chopra, N.; Higgs, C.; Kasavajhala, K.; Li, H.; Nandekar, P.; et al. Benchmarking Refined and Unrefined AlphaFold2 Structures for Hit Discovery. *Journal of Chemical Information and Modeling* **2023**, *63*, 1656-1667, doi:10.1021/acs.jcim.2c01219.

45. Melesina, J.; Simoben, C.V.; Praetorius, L.; Bülbül, E.F.; Robaa, D.; Sippl, W. Strategies To Design Selective Histone Deacetylase Inhibitors. *ChemMedChem* **2021**, *16*, 1336-1359, doi:10.1002/cmdc.202000934.

46. Zhang, L.; Zhang, J.; Jiang, Q.; Zhang, L.; Song, W. Zinc binding groups for histone deacetylase inhibitors. *J Enzyme Inhib Med Chem* **2018**, *33*, 714-721, doi:10.1080/14756366.2017.1417274.

47. De Vreese, R.; D'Hooghe, M. Synthesis and applications of benzohydroxamic acid-based histone deacetylase inhibitors. *Eur J Med Chem* **2017**, *135*, 174-195, doi:10.1016/j.ejmech.2017.04.013.

48. Hu, Z.; Wei, F.; Su, Y.; Wang, Y.; Shen, Y.; Fang, Y.; Ding, J.; Chen, Y. Histone deacetylase inhibitors promote breast cancer metastasis by elevating NEDD9 expression. *Signal Transduction and Targeted Therapy* **2023**, *8*, 11, doi:10.1038/s41392-022-01221-6.

49. Irwin, J.J.; Tang, K.G.; Young, J.; Dandarchuluun, C.; Wong, B.R.; Khurelbaatar, M.; Moroz, Y.S.; Mayfield, J.; Sayle, R.A. ZINC20—A Free Ultralarge-Scale Chemical Database for Ligand Discovery. *Journal of Chemical Information and Modeling* **2020**, *60*, 6065-6073, doi:10.1021/acs.jcim.0c00675.

50. Lipinski, C.A.; Lombardo, F.; Dominy, B.W.; Feeney, P.J. Experimental and computational approaches to estimate solubility and permeability in drug discovery and development settings. *Adv Drug Deliv Rev* **2001**, *46*, 3-26, doi:10.1016/s0169-409x(00)00129-0.

51. Kumari, S.; Chakraborty, S.; Ahmad, M.; Kumar, V.; Tailor, P.B.; Biswal, B.K. Identification of probable inhibitors for the DNA polymerase of the Monkeypox virus through the virtual screening approach. *Int J Biol Macromol* **2023**, *229*, 515-528, doi:10.1016/j.ijbiomac.2022.12.252.

52. Walters, W.P.; Stahl, M.T.; Murcko, M.A. Virtual screening—an overview. *Drug Discovery Today* **1998**, *3*, 160-178, doi:https://doi.org/10.1016/S1359-6446(97)01163-X.

53. Walters, W.P.; Namchuk, M. Designing screens: how to make your hits a hit. *Nat Rev Drug Discov* **2003**, *2*, 259-266, doi:10.1038/nrd1063.

54. Dan, A.; Shiyama, T.; Yamazaki, K.; Kusunose, N.; Fujita, K.; Sato, H.; Matsui, K.; Kitano, M. Discovery of hydroxamic acid analogs as dual inhibitors of phosphodiesterase-1 and -5. *Bioorg Med Chem Lett* **2005**, *15*, 4085-4090, doi:10.1016/j.bmcl.2005.06.016.

55. Heimburg, T.; Kolbinger, F.R.; Zeyen, P.; Ghazy, E.; Herp, D.; Schmidtkunz, K.; Melesina, J.; Shaik, T.B.; Erdmann, F.; Schmidt, M.; et al. Structure-Based Design and Biological Characterization of Selective Histone Deacetylase 8 (HDAC8) Inhibitors with Anti-Neuroblastoma Activity. *Journal of Medicinal Chemistry* **2017**, *60*, 10188-10204, doi:10.1021/acs.jmedchem.7b01447.

56. Marek, M.; Ramos-Morales, E.; Picchi-Constante, G.F.A.; Bayer, T.; Norström, C.; Herp, D.; Sales-Junior, P.A.; Guerra-Slompo, E.P.; Hausmann, K.; Chakrabarti, A.; et al. Species-selective targeting of pathogens revealed by the atypical

783 structure and active site of Trypanosoma cruzi histone deacetylase DAC2. *Cell Rep* **2021**, *37*, 110129,
784 doi:10.1016/j.celrep.2021.110129.
785 57. Barducci, A.; Bonomi, M.; Parrinello, M. Metadynamics. *WIREs Computational Molecular Science* **2011**, *1*, 826-843,
786 doi:https://doi.org/10.1002/wcms.31.
787 58. Fusani, L.; Palmer, D.S.; Somers, D.O.; Wall, I.D. Exploring Ligand Stability in Protein Crystal Structures Using
788 Binding Pose Metadynamics. *Journal of Chemical Information and Modeling* **2020**, *60*, 1528-1539, doi:10.1021/acs.jcim.9b00843.
789 59. Clark, A.J.; Tiwary, P.; Borrelli, K.; Feng, S.; Miller, E.B.; Abel, R.; Friesner, R.A.; Berne, B.J. Prediction of
790 Protein–Ligand Binding Poses via a Combination of Induced Fit Docking and Metadynamics Simulations. *Journal of Chemical*
791 *Theory and Computation* **2016**, *12*, 2990-2998, doi:10.1021/acs.jctc.6b00201.
792 60. *Schrödinger Release 2019-1: Maestro, Schrödinger, LLC, New York, NY, 2019.*
793 61. Sastry, G.M.; Adzhigirey, M.; Day, T.; Annabhimoju, R.; Sherman, W. Protein and ligand preparation:
794 parameters, protocols, and influence on virtual screening enrichments. *J Comput Aided Mol Des* **2013**, *27*, 221-234,
795 doi:10.1007/s10822-013-9644-8.
796 62. *Schrödinger Release 2019-1: Protein Preparation Wizard; Epik, Schrödinger, LLC, New York, NY,*
797 *2019; Impact, Schrödinger, LLC, New York, NY, 2019; Prime, Schrödinger, LLC, New York, NY, 2019.*
798 63. Jacobson, M.P.; Pincus, D.L.; Rapp, C.S.; Day, T.J.; Honig, B.; Shaw, D.E.; Friesner, R.A. A hierarchical approach
799 to all-atom protein loop prediction. *Proteins* **2004**, *55*, 351-367, doi:10.1002/prot.10613.
800 64. Jacobson, M.P.; Friesner, R.A.; Xiang, Z.; Honig, B. On the role of the crystal environment in determining
801 protein side-chain conformations. *J Mol Biol* **2002**, *320*, 597-608, doi:10.1016/s0022-2836(02)00470-9.
802 65. *Schrödinger Release 2019-1: Prime, Schrödinger, LLC, New York, NY, 2019*.
803 66. Greenwood, J.R.; Calkins, D.; Sullivan, A.P.; Shelley, J.C. Towards the comprehensive, rapid, and accurate
804 prediction of the favorable tautomeric states of drug-like molecules in aqueous solution. *J Comput Aided Mol Des* **2010**, *24*,
805 591-604, doi:10.1007/s10822-010-9349-1.
806 67. Shelley, J.C.; Cholleti, A.; Frye, L.L.; Greenwood, J.R.; Timlin, M.R.; Uchimaya, M. Epik: a software program for
807 pK(a) prediction and protonation state generation for drug-like molecules. *J Comput Aided Mol Des* **2007**, *21*, 681-691,
808 doi:10.1007/s10822-007-9133-z.
809 68. *Schrödinger Release 2019-1: Epik, Schrödinger, LLC, New York, NY, 2019*.
810 69. Ghazy, E.; Heimburg, T.; Lancelot, J.; Zeyen, P.; Schmidtkunz, K.; Truhn, A.; Darwish, S.; Simoben, C.V.; Shaik,
811 T.B.; Erdmann, F.; et al. Synthesis, structure-activity relationships, cocrystallization and cellular characterization of novel
812 smHDAC8 inhibitors for the treatment of schistosomiasis. *European Journal of Medicinal Chemistry* **2021**, *225*, 113745,
813 doi:https://doi.org/10.1016/j.ejmech.2021.113745.
814 70. Ghazy, E.; Zeyen, P.; Herp, D.; Hügle, M.; Schmidtkunz, K.; Erdmann, F.; Robaa, D.; Schmidt, M.; Morales, E.R.;
815 Romier, C.; et al. Design, synthesis, and biological evaluation of dual targeting inhibitors of histone deacetylase 6/8 and
816 bromodomain BRPF1. *European Journal of Medicinal Chemistry* **2020**, *200*, 112338,
817 doi:https://doi.org/10.1016/j.ejmech.2020.112338.
818 71. Marek, M.; Shaik, T.B.; Heimburg, T.; Chakrabarti, A.; Lancelot, J.; Ramos-Morales, E.; Da Veiga, C.; Kalinin, D.;
819 Melesina, J.; Robaa, D.; et al. Characterization of Histone Deacetylase 8 (HDAC8) Selective Inhibition Reveals Specific Active
820 Site Structural and Functional Determinants. *Journal of Medicinal Chemistry* **2018**, *61*, 10000-10016,
821 doi:10.1021/acs.jmedchem.8b01087.
822 72. Vögerl, K.; Ong, N.; Senger, J.; Herp, D.; Schmidtkunz, K.; Marek, M.; Müller, M.; Bartel, K.; Shaik, T.B.; Porter,
823 N.J.; et al. Synthesis and Biological Investigation of Phenothiazine-Based Benzhydroxamic Acids as Selective Histone
824 Deacetylase 6 Inhibitors. *Journal of Medicinal Chemistry* **2019**, *62*, 1138-1166, doi:10.1021/acs.jmedchem.8b01090.

73. *Schrödinger Release 2019-1: LigPrep, Schrödinger, LLC, New York, NY, 2019*.

74. Harder, E.; Damm, W.; Maple, J.; Wu, C.; Reboul, M.; Xiang, J.Y.; Wang, L.; Lupyan, D.; Dahlgren, M.K.; Knight, J.L.; et al. OPLS3: A Force Field Providing Broad Coverage of Drug-like Small Molecules and Proteins. *J Chem Theory Comput* **2016**, *12*, 281-296, doi:10.1021/acs.jctc.5b00864.

75. Shivakumar, D.; Williams, J.; Wu, Y.; Damm, W.; Shelley, J.; Sherman, W. Prediction of Absolute Solvation Free Energies using Molecular Dynamics Free Energy Perturbation and the OPLS Force Field. *Journal of Chemical Theory and Computation* **2010**, *6*, 1509-1519, doi:10.1021/ct900587b.

76. Jorgensen, W.L.; Maxwell, D.S.; Tirado-Rives, J. Development and Testing of the OPLS All-Atom Force Field on Conformational Energetics and Properties of Organic Liquids. *Journal of the American Chemical Society* **1996**, *118*, 11225-11236, doi:10.1021/ja9621760.

77. Jorgensen, W.L.; Tirado-Rives, J. The OPLS [optimized potentials for liquid simulations] potential functions for proteins, energy minimizations for crystals of cyclic peptides and crambin. *Journal of the American Chemical Society* **1988**, *110*, 1657-1666, doi:10.1021/ja00214a001.

78. *Schrödinger Release 2019-1: QikProp, Schrödinger, LLC, New York, NY, 2019*.

79. Salam, N.K.; Nuti, R.; Sherman, W. Novel method for generating structure-based pharmacophores using energetic analysis. *J Chem Inf Model* **2009**, *49*, 2356-2368, doi:10.1021/ci900212v.

80. Loving, K.; Salam, N.K.; Sherman, W. Energetic analysis of fragment docking and application to structure-based pharmacophore hypothesis generation. *J Comput Aided Mol Des* **2009**, *23*, 541-554, doi:10.1007/s10822-009-9268-1.

81. Dixon, S.L.; Smondyrev, A.M.; Knoll, E.H.; Rao, S.N.; Shaw, D.E.; Friesner, R.A. PHASE: a new engine for pharmacophore perception, 3D QSAR model development, and 3D database screening: 1. Methodology and preliminary results. *J Comput Aided Mol Des* **2006**, *20*, 647-671, doi:10.1007/s10822-006-9087-6.

82. Dixon, S.L.; Smondyrev, A.M.; Rao, S.N. PHASE: A Novel Approach to Pharmacophore Modeling and 3D Database Searching. *Chemical Biology & Drug Design* **2006**, *67*, 370-372, doi:https://doi.org/10.1111/j.1747-0285.2006.00384.x.

83. *Schrödinger Release 2019-1: Phase, Schrödinger, LLC, New York, NY, 2019*.

84. Friesner, R.A.; Murphy, R.B.; Repasky, M.P.; Frye, L.L.; Greenwood, J.R.; Halgren, T.A.; Sanschagrin, P.C.; Mainz, D.T. Extra precision glide: docking and scoring incorporating a model of hydrophobic enclosure for protein-ligand complexes. *J Med Chem* **2006**, *49*, 6177-6196, doi:10.1021/jm051256o.

85. Friesner, R.A.; Banks, J.L.; Murphy, R.B.; Halgren, T.A.; Klicic, J.J.; Mainz, D.T.; Repasky, M.P.; Knoll, E.H.; Shelley, M.; Perry, J.K.; et al. Glide: a new approach for rapid, accurate docking and scoring. 1. Method and assessment of docking accuracy. *J Med Chem* **2004**, *47*, 1739-1749, doi:10.1021/jm0306430.

86. Halgren, T.A.; Murphy, R.B.; Friesner, R.A.; Beard, H.S.; Frye, L.L.; Pollard, W.T.; Banks, J.L. Glide: A New Approach for Rapid, Accurate Docking and Scoring. 2. Enrichment Factors in Database Screening. *Journal of Medicinal Chemistry* **2004**, *47*, 1750-1759, doi:10.1021/jm030644s.

87. *Schrödinger Release 2019-1: Glide, Schrödinger, LLC, New York, NY, 2019*.

88. Duan, J.; Dixon, S.L.; Lowrie, J.F.; Sherman, W. Analysis and comparison of 2D fingerprints: insights into database screening performance using eight fingerprint methods. *J Mol Graph Model* **2010**, *29*, 157-170, doi:10.1016/j.jmgm.2010.05.008.

89. Sastry, M.; Lowrie, J.F.; Dixon, S.L.; Sherman, W. Large-Scale Systematic Analysis of 2D Fingerprint Methods and Parameters to Improve Virtual Screening Enrichments. *Journal of Chemical Information and Modeling* **2010**, *50*, 771-784, doi:10.1021/ci100062n.

90. *Schrödinger Release 2019-1: Canvas, Schrödinger, LLC, New York, NY, 2019*.

91. Bowers, K.J.; Chow, D.E.; Xu, H.; Dror, R.O.; Eastwood, M.P.; Gregersen, B.A.; Klepeis, J.L.; Kolossvary, I.; Moraes, M.A.; Sacerdoti, F.D.; et al. Scalable Algorithms for Molecular Dynamics Simulations on Commodity Clusters. In Proceedings of the SC '06: Proceedings of the 2006 ACM/IEEE Conference on Supercomputing, 11-17 Nov. 2006, 2006; pp. 43-43.

92. *Schrödinger Release 2019-1; Desmond Molecular Dynamics System, D.E. Shaw Research: New York, NY, USA, 2019; Maestro-Desmond Interoperability Tools, Schrödinger: New York, NY, USA, 2019*.

93. Zessin, M.; Kutil, Z.; Meleshin, M.; Nováková, Z.; Ghazy, E.; Kalbas, D.; Marek, M.; Romier, C.; Sippl, W.; Bařinka, C.; et al. One-Atom Substitution Enables Direct and Continuous Monitoring of Histone Deacylase Activity. *Biochemistry* **2019**, *58*, 4777-4789, doi:10.1021/acs.biochem.9b00786.